

1 Using feature-based verification methods to explore the spatial and 2 temporal characteristics of the 2019 Chlorophyll-*a* bloom season in a 3 model of the European North-West Shelf

4 Marion Mittermaier¹, Rachel North¹, Jan Maksymczuk², Christine Pequignet², David Ford²

5 ¹Verification, Impacts and Post-Processing, Weather Science, Met Office, Exeter, EX1 3PB, United Kingdom

6 ²Ocean Forecasting Research & Development, Weather Science, Met Office, Exeter, EX1 3PB, United Kingdom

7
8 *Correspondence to:* Marion Mittermaier (marion.mittermaier@metoffice.gov.uk)

9 **Abstract.**

10 Two feature-based verification methods, thus far only used for the diagnostic evaluation of atmospheric
11 ~~model applications~~models, have been applied to compare ~7 km resolution pre-operational analyses of
12 Chlorophyll-*a* (Chl-*a*) concentrations ~~from the Met Office Atlantic Margin Model at 7 km resolution~~
13 ~~(AMM7v11) for the North West European Shelf Seas with~~to a 1 km gridded ~~-~~satellite-derived Chl-*a*
14 concentrations product ~~from the Copernicus Marine Environment Monitoring Service (CMEMS)~~
15 ~~catalogue.~~ The aim of this study was to assess the value of applying such methods to ocean models.
16 Chl-*a* bloom objects were identified using a range of thresholds in both datasets for the 2019 bloom
17 season (March 1 to 31 July). These bloom objects were analysed as purely discrete (2D) spatial features
18 and, but also as space-time ~~objects, enabling the ability to define~~(3D) features, providing the means of
19 defining the onset, duration, and demise of distinct bloom episodes. ~~Overall, and the AMM7v11 season~~
20 as a whole.
21 ~~The model analyses were found to be similar to the satellite product. The AMM7v11 analyses were not~~
22 ~~always~~ are not able to represent small coastal bloom objects, given the ~~coastline~~coarser definition ~~in a~~
23 ~~~7 km model and sub-grid scale processes. By contrast of~~ the ~~AMM7v11 coastline.~~ The analyses
24 ~~produces also wrongly produce~~ more bloom objects in deeper Atlantic waters, ~~which are not detected by~~
25 ~~the satellite product.~~ Concentrations in the ~~AMM7v11 model~~ analyses are somewhat higher overall.
26 ~~This~~The bias manifests itself in the size of the ~~AMM7v11 model analysis~~ bloom objects, which tend to
27 be larger than the satellite-derived bloom objects ~~identified in the satellite product~~. Based on this

28 ~~analysis—these feature-based methods~~ the onset of the bloom season is delayed by 26 days in the
29 ~~AMM7v11model analyses~~, but the season also persists for another month beyond the diagnosed end.
30 ~~Overall, the~~The season was diagnosed to be 119 days long, ~~based on the AMM7v11 space-time objects,~~
31 ~~and— in the model analyses, compared to~~ 117 days from the satellite product. Geographically the
32 ~~AMM7v11model analyses~~ and satellite ~~product-derived bloom~~ objects ~~do overlap at times, but further~~
33 ~~analysis shows they~~ do not necessarily exist in ~~that a~~ specific location at the same time, ~~and only overlap~~
34 ~~occasionally~~.

35 **1 Introduction**

36 The advancements in atmospheric numerical weather prediction (NWP) such as the improvements in
37 model resolution began to expose the relative weaknesses in so-called traditional verification scores
38 (such as the root-mean-squared-error for example), which rely on the precise matching in space and
39 time of the forecast to a suitable observation. These metrics and measures no longer provided adequate
40 information to quantify forecast performance (e.g. Mass et al. 2002). One key characteristic of high-
41 resolution forecasts is the apparent detail they provide, but this detail may not be in the right place at the
42 right time, a phenomenon referred to as the “double penalty effect” (Rossa et al., 2008). Essentially it
43 means that at any given time the error is counted twice because the forecast occurred where it was not
44 observed, and it did not occur where it was observed. This realisation created the need within the
45 atmospheric community for creating more informative yet robust verification methods. As a result, a
46 multitude of so-called “spatial” verification methods were developed, which essentially provide a
47 number of ways for accounting for the characteristics of high-resolution forecasts.

48

49 In 2007 a spatial verification method inter-comparison (Gilleland et al., 2009, 2010) was established
50 with the aim of providing a better collective understanding of what each of the new methods was
51 designed for, and categorising what type of forecast errors each could quantify. A decade later
52 Dorninger et al. (2018) revisited this inter-comparison, adding a fifth category so that all spatial
53 methods fall into one of the following groupings: neighbourhood, scale separation, feature-based,
54 distance metrics or field deformation.

55

56 The use of spatial verification methods has therefore become commonplace for atmospheric NWP (see
57 Dorninger et al. (2018) and references within). Neighbourhood-based methods in particular have
58 become popular due to the relative ease of computation and intuitive interpretation. Recently one such
59 neighbourhood spatial method was demonstrated as an effective approach for exploring the benefit of
60 higher resolution ocean forecasts (Crocker et al., 2020). Another class of methods focus on how well
61 particular features of interest are being forecast. Forecasting specific features of interest is one of the
62 main reasons for increasing horizontal resolution. Feature-based verification methods, such as the
63 Method for Object-based Diagnostic Evaluation (MODE, Davis et al., 2006) and the time domain
64 version MODE-TD (Clark et al., 2014) enable an assessment of such features, focusing on the physical
65 attributes of the features (identified using a threshold) and how they behave at a given point in time, and
66 evolve over time. These methods require a gridded truth to compare to. Whilst the initial inter-
67 comparison project was based on analysing precipitation forecasts, over recent years their use has
68 extended to other variables, provided gridded data sets exist that can be used to compare against (e.g.
69 Crocker & Mittermaier (2013) considered cloud masks and Mittermaier et al., (2016) considered more
70 continuous fields in a global NWP model such as upper-level jet cores, surface lows and high pressure
71 cells using model analyses-). Mittermaier & Bullock (2013) detailed the first study to use MODE-TD
72 prototype tools to analyse the evolution of cloud breaks over the UK using satellite-derived cloud
73 analyses.

74

75 In the ocean, several processes have strong visual signatures that can be detected by satellite sensors.
76 For example, mesoscale eddies can be detected from sea surface temperature or sea level anomaly (e.g.
77 (Chelton et al., 2011, Morrow and Le Traon, 2012, Hausmann and Czaja, 2012)). Phytoplankton blooms
78 are seasonal events which see rapid phytoplankton growth as a result of changing ocean mixing,
79 temperature and light conditions (Sverdrup, 1953, Winder and Cloern, 2010, Chiswell, 2011)). Blooms
80 represent an important contribution to the oceanic primary production-~~that is,~~ a key process for the
81 oceanic carbon cycle (Falkowski et al., 1998). Their spatial extent and intensity in the upper ocean make
82 them visible from space with ocean colour sensors (Gordon et al., 1983, Behrenfeld et al., 2005).

83 Biogeochemical models coupled to physical models of the ocean provide simulations for the various
84 parameters that ~~characterise~~characterize the evolution of a spring bloom. ~~In particular, Chlorophyll-*a*~~
85 ~~(Chl-*a*) concentrations provide an index of phytoplankton biomass., such as~~ Chl-*a* concentration which
86 can also be estimated from spaceborne ocean colour sensors (Antoine et al., 1996).

87
88 Validation of marine biogeochemical models has traditionally relied on simple statistical comparisons
89 with observation products, often limited to visual inspections (Stow et al., 2009; Hipsey et al., 2020). In
90 response to this, various papers have outlined and advocated using a hierarchy of statistical techniques
91 (Allen et al., 2007a, 2007b; Stow et al., 2009; Hipsey et al., 2020), multivariate approaches (Allen and
92 Somerfield, 2009), and novel diagrams (Jolliff et al., 2009). Many of these rely on matching to
93 observations in space and time, but some studies have started applying feature-based verification
94 methods: ~~((Mattern, et al.2010))~~. Emergent properties have been assessed in terms of geographical
95 provinces (Vichi et al., 2011), phenological indices (Anugerahanti et al., 2018), and ecosystem
96 functions ~~(De Mora et al., 2016)~~(de Mora et al., 2016). In a previous application of spatial verification
97 methods developed for NWP, ~~Saux Picart et al., 2012~~Saux Picart et al. (2012) used a wavelet-based
98 method to compare Chl-*a* concentrations from a model of the European North West Shelf to an ocean
99 colour product.

100

101 For this paper, both MODE and MODE-TD (or MTD for short) were applied to the latest pre-
102 operational analysis (at the time) of the Met Office Atlantic Margin Model (AMM7) at 7 km resolution
103 (O’Dea et al., 2012; Edwards et al., 2012; O’Dea et al., 2017; ~~King et al., 2018~~)King et al., 2018;
104 (McEwan et al., 2021)) for the European North West Shelf (NWS), in order to evaluate the spatio-
105 temporal evolution of the bloom season in both model and observation fields. ~~A traditional verification~~
106 ~~of the system (e.g. using root mean squared error and similar metrics) is out of scope of this study and~~
107 ~~will be presented in a separate publication.~~A full traditional verification of the system (e.g. using root-
108 mean-squared-error and similar metrics) is out of scope of this study and will be presented in a separate
109 publication. For comparison with the MODE and MTD results, a few traditional metrics are included
110 here, based on the Copernicus Marine Environment Monitoring Service (CMEMS) Quality Information

111 [Document for the model \(McEwan et al., 2021\)](#). Traditional verification of a previous version, prior to
112 the introduction of ocean colour data assimilation, was presented by Edwards et al. (2012), who used
113 various metrics and Taylor diagrams (Taylor, 2001) to compare model analyses to satellite and in-situ
114 observations. Ford et al. (2017) presented further validation, to understand the skill of the model at
115 representing phytoplankton community structure in the North Sea. A similar version of the system used
116 in this study, including ocean colour data assimilation, was assessed in Skákala et al. (2018), who
117 validated both analysis and forecast skill using traditional methods. The assimilation improved analysis
118 and forecast skill compared with the free-running model, but when assessed against satellite ocean
119 colour the forecasts were not found to beat persistence. On the NWS the spring bloom usually begins
120 between February and April, varying across the domain and interannually (Siegel et al., 2002; Smyth et
121 al., 2014), and lasts until summer. Without data assimilation the spring bloom in the model typically
122 occurs later than in observations (Skákala et al., 2018, 2020), a bias which is largely corrected by
123 assimilating ocean colour data.

124

125 In Section 2 the data sets used in the verification process are introduced. Section 3 describes MODE and
126 MTD. Section 4 contains a selection of results, and their interpretation. Conclusions and
127 recommendations follow in Section 5.

128 **2 Data sets for the 2019 Chl-*a* bloom**

129 As stated in Section 1, feature-based methods such as MODE and MTD require the fields to be
130 compared to be on the same grid. [The model grid is used here.](#)

131 **2.1 Satellite-derived gridded ocean colour products**

132 A cloud-free gridded (space-time interpolated, L4) daily product delivered through the Copernicus
133 Marine Environment Monitoring Service (CMEMS, Le Traon et al., 2019) catalogue provides Chl-*a*
134 concentration at ~1 km resolution over the Atlantic (46°W–13°E, 20°N–66°N). The L4 Chl-*a* product is
135 derived from merging of data from multiple satellite-borne sensors: MODIS-Aqua, VIIRSN and OLCI-
136 S3A. The reprocessed (REP) products available nearly 6 months after the measurements

137 (OCEANCOLOUR_ATL_CHL_L4_REP_OBSERVATIONS_009_091098) are used here as it is the
138 best-quality gridded product available for comparison. The satellite derived ~~chlorophyll~~Chl-*a*
139 concentration estimate is an integrated value over optical depth.

140

141 Errors in satellite-derived Chl-*a* can be more than 100% of the observed value (e.g. Moore et al., 2009).
142 The errors in the L4 Chl-*a* values are often at their largest near the coast, especially near river outflows.
143 However, in the rest of the domain, smaller values of Chl-*a* mean that even large percentage
144 observation errors result in errors typically smaller than the difference between model and observations.
145 As will be shown, the models at 7 km resolution cannot resolve the coasts in the same way as is seen in
146 the satellite product as some of the coastal Chl-*a* dynamics are sub-grid scale for a 7 km resolution
147 model.

148

149 For this study the ~1 km resolution L4 satellite product was interpolated onto the AMM7 grid using
150 standard two-dimensional horizontal cubic interpolation. This coarsening process retained some of the
151 larger concentrations present in the L4 product.

152 **2.2 Model description**

153 Operational modelling of the NWS is performed using the Forecast Ocean Assimilation Model (FOAM)
154 system. This consists of the NEMO (Nucleus for European Modelling of the Ocean) hydrodynamic
155 model (Madec et al., 2016; O'Dea et al., 2017), the NEMOVAR data assimilation scheme (Waters et al.,
156 2015; King et al., 2018), and for the NWS region the European Regional Seas Ecosystem Model
157 (ERSEM), which provides forecasts for the lower trophic levels of the marine food web (Butenschön et
158 al., 2016). The version of FOAM used in this study is AMM7v11, using the ~7 km horizontal
159 resolution domain stretching from 40 °N, 20 °W to 65 °N, 13 °E. Operational forecasts of ocean physics
160 and biogeochemistry for the NWS are delivered through CMEMS, for a summary of the principles
161 underlying the service see e.g. Le Traon et al. (2019).

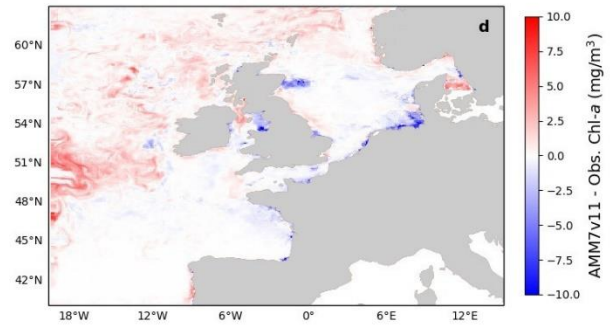
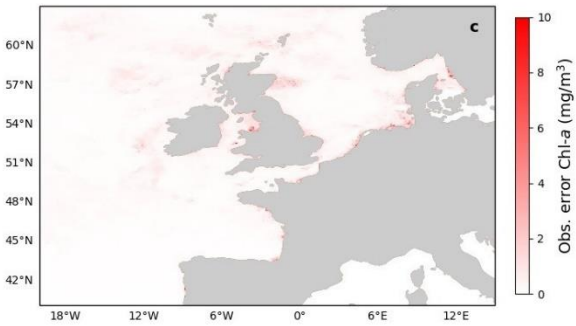
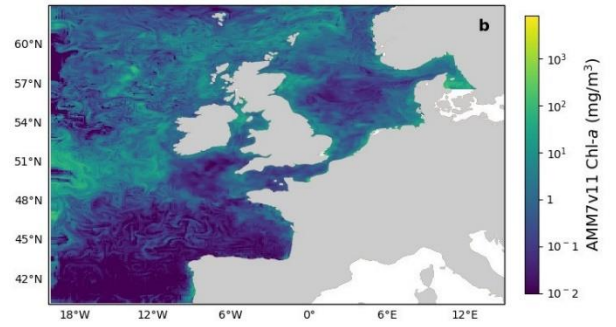
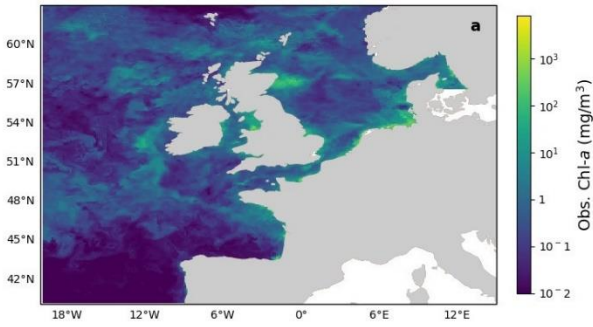
162

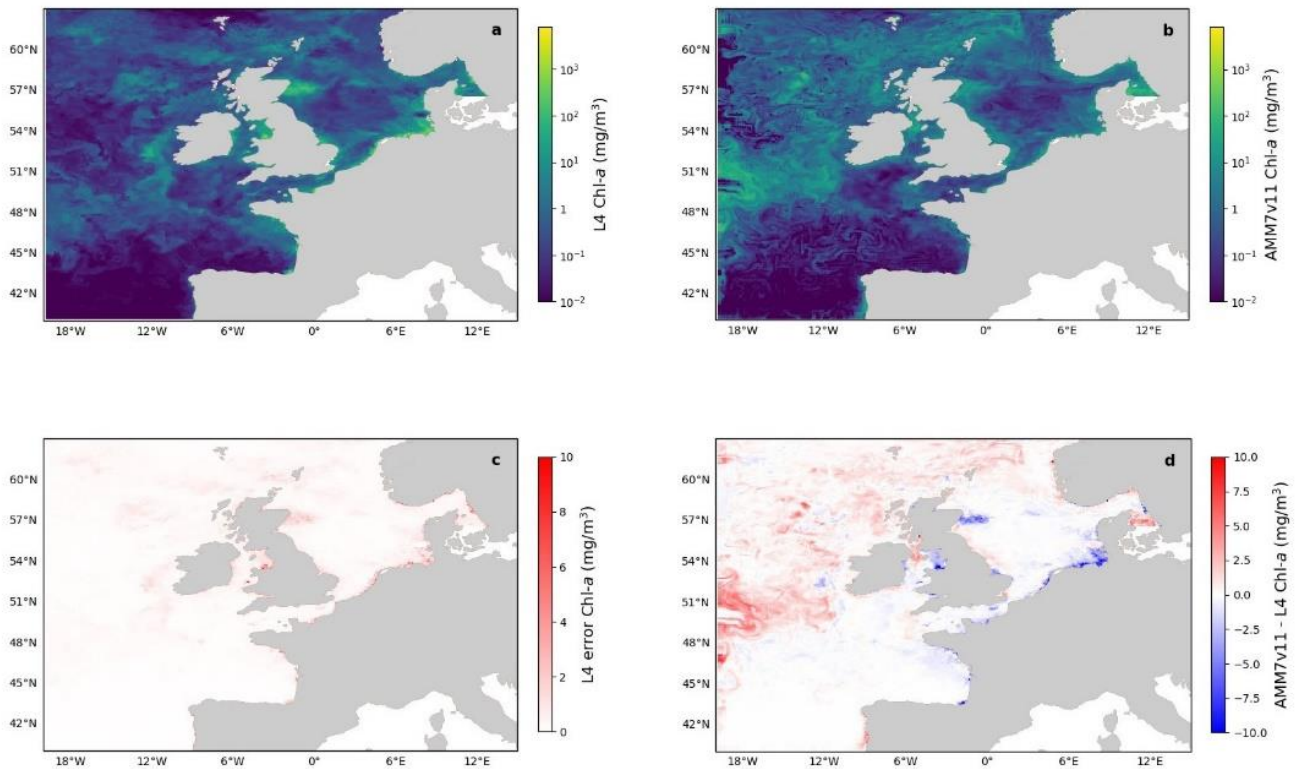
163 AMM7v11 uses the CO6 configuration of NEMO, which is configured for the shallow water of the
164 shelf sea and is a development of the CO5 configuration described by O'Dea et al. (2017). The ERSEM
165 version used is v19.04, coupled to NEMO using the Framework for Aquatic Biogeochemical Models
166 (FABM, Bruggeman and Bolding, 2014). The NEMOVAR version is v6.0, with a 3D-Var method used
167 to assimilate satellite and in situ sea surface temperature (SST) observations, in situ temperature and
168 salinity profiles, and altimetry data into NEMO (King et al., 2018), and chlorophyll derived from
169 satellite ocean colour into ERSEM (Skákala et al., 2018). The introduction of ocean colour assimilation
170 in AMM7v11 is a major development for the biogeochemistry over previous versions of the system
171 (Edwards et al., 2012). The satellite ocean colour observations assimilated are from a daily L3 multi-
172 sensor composite product based on MODIS and VIIRS with resolutions of 1 km for the Atlantic (for
173 further information see OCEANCOLOUR_ATL_CHL_L3_NRT_OBSERVATIONS_009_036 on the
174 CMEMS catalogue). The L3 product is based on two of the same three ocean colours sensors used in
175 the L4 product described in Section 2.1, but with different processing and no gap-filling.
176

177 In this study daily mean Chl-*a* concentrations for the period of 1 March-31 July 2019 from AMM7v11
178 were used to illustrate the verification methodology. AMM7v11 entered operational use in December
179 2020, and the data used here came from a pre-operational run of the system. Note only the analysis of
180 AMM7v11 (i.e. no corresponding forecasts) was available at the time of the assessment, and the results
181 presented in this paper show how close the data assimilation draws the model to the observed state.

182 **2.3 Visual inspection of data sets**

183 Ideally, Chl-*a* concentration from the model should be integrated over optical depth to be equivalent to
184 the satellite derived value defined in Section 2.1 (Dutkiewicz et al., 2018). However, this is currently a
185 non-trivial exercise, and cannot be accurately calculated from offline outputs. Therefore, the commonly
186 accepted practice is to use the model surface Chl-*a* (Lorenzen, 1970, (Shutler et al., 2011). Here it is
187 assumed that the difference between surface and optical depth-integrated Chl-*a* is likely to be small in
188 comparison with the actual model errors.





190

191 **Figure 1 (a) Daily mean L4 multi-sensor observations regrided on the 7 km resolution model grid and (b) AMM7v11**
 192 **Chl-*a* for 1 June 2019. (c) Error estimates on the multi-sensor L4 Chl-*a* and (d) difference between AMM7v11 and**
 193 **the L4 product.**

194

195 Figure 1 shows the L4 ocean colour product (a) and AMM7v11 analysis (b) for 1 June 2019 on the top
 196 row, using the same plotting ranges. The second row shows the difference field that is provided with the
 197 L4 ocean colour product (c), and the AMM7v11 minus L4 difference field (d). The mean error (bias) is
 198 generally positive with the AMM7v11 analysis containing higher Chl-*a* concentrations, especially in the
 199 deeper North Atlantic waters. The exceptions are along the coast where the AMM7v11 analysis is
 200 deficient, but it should be noted that these are also the zones where some of the largest satellite retrieval
 201 errors occur and where a 7-km resolution model, with a coarse representation of the coast, does not fully
 202 represent complex coastal and estuarine processes.

203 3 Method for Object-based Diagnostic Evaluation (MODE) and MODE Time-Domain (MTD)

204 3.1. Description of the methods

205 This section provides a brief description of the Method for Object-Based Diagnostic Evaluation
206 (MODE), first described in Davis et al. (2006) and its extension MODE Time-Domain (MTD).

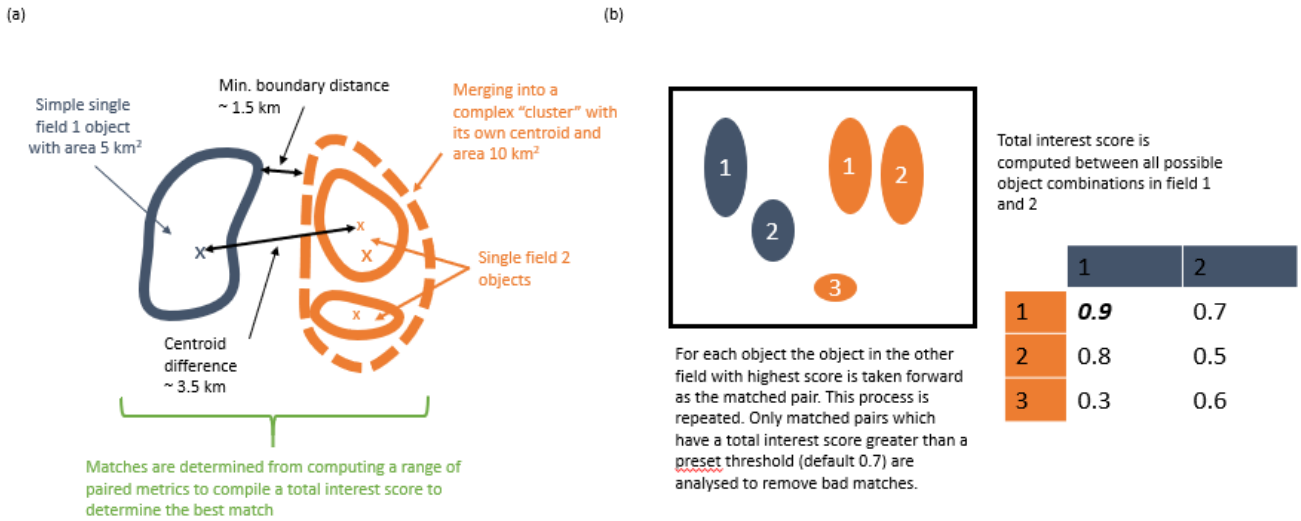
207

208 MODE and MTD can be used on any temporal sequence of two gridded data sets which contain features
209 that are of interest to a user (whoever that user may be, model developer or more applied). By extracting
210 only the feature(s) of interest, the method allows one to mimic what humans do, but in an objective
211 way. Once identified the features can then be mathematically analysed over many days or seasons to
212 compute aggregate statistics of behaviour. MODE can be used in a very generalised way. The key
213 requirements are to 1) have gridded fields to compare and 2) be able to set a threshold for identifying
214 features of interest.

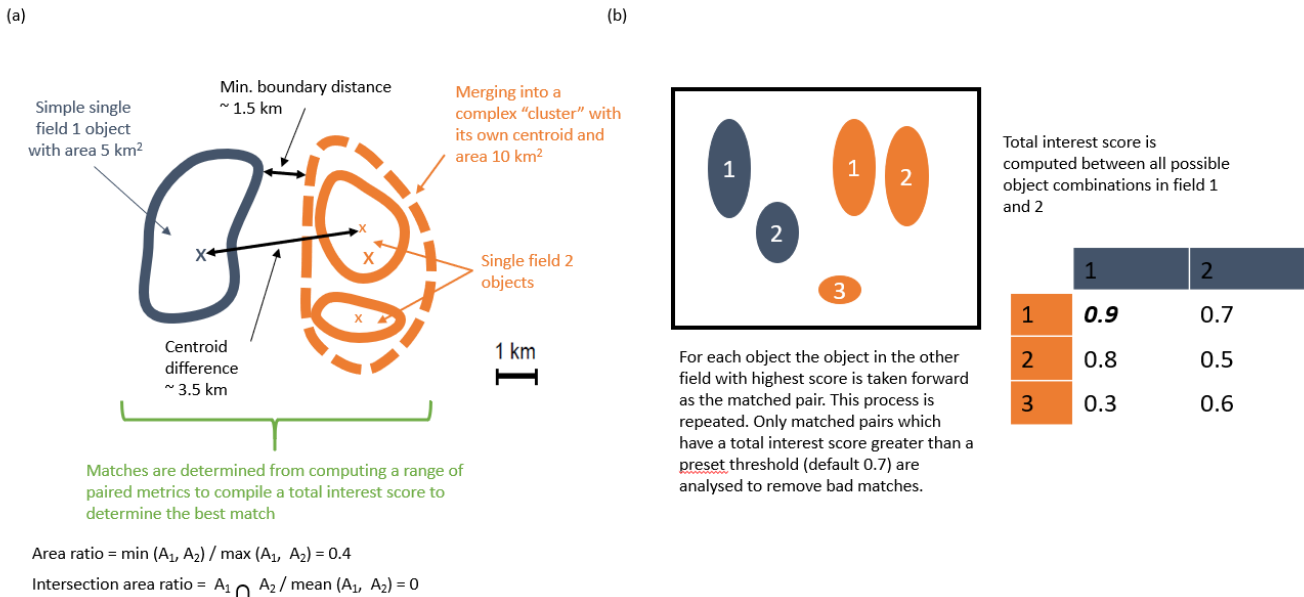
215

216 In this instance the comparison will involve the AMM7v11 model data assimilation analysis and the
217 gridded L4 satellite product. MODE identifies the features (called objects), as areas for which a
218 specified threshold is exceeded, here it is a Chl-*a* concentration. Consider Figure 2 which shows a
219 number of objects that have been identified after a threshold has been applied to two fields (blue and
220 orange). The identified objects in the two fields are of different sizes and shapes and do not overlap in
221 space, though they are not far apart. Object characteristics or attributes such as the area and mass-
222 weighted centroid are computed for each single object. Simple (also known as single) objects can be
223 *merged* (to form clusters) within *one* field (illustrated here for the orange field). This may be useful to
224 do if it is clear that there are many small objects close together which should really be treated as one.
225 Furthermore, objects in one field can be *matched* to objects in the other field. To find the best match an
226 interest score is computed for each possible pairing: between all identified objects. The components
227 used for computing the interest score can be tuned to meet specific user needs. ~~In~~ In Figure 2(a) it is
228 based on the area ratio, intersection-area ratio, minimum boundary distance and centroid difference.
229 Furthermore, the components can be weighted according to relative importance. Given a scenario where
230 there are 2 identified objects in the blue field and 3 in the orange field (Figure 2(b) shows the interest

231 score for each possible pairing in this hypothetical example. Only the pairing with the highest score is
232 analysed further, and only if it exceeds the set threshold for defining an acceptable match. The default
233 value for this is 0.7. ~~Once these matches are completed summary statistics describing the~~For the
234 example blue object 1 is best matched against orange object 1, and this match is used in the analysis.
235 Note that there is another good match with orange object 2 as it is above the threshold of 0.7, but it, as
236 well as the orange object 3 would not be used, with orange object 3 below the 0.7 threshold. In all
237 likelihood a scenario such as shown in Figure 2(b) would be assessed as clusters with blue objects 1 and
238 2 forming a cluster and orange objects 1 and 2 also forming a cluster. An interest score for the cluster
239 pairing above 0.7 would then create a matched pair. Once these matches are completed summary
240 statistics describing the individual objects (both matched and unmatched) and matched object pairs are
241 produced. These statistics can be used to identify similarities and differences between the objects
242 identified in two different data sets, which can provide diagnostic insights on the relative strengths and
243 weaknesses of one compared to the other.



244



245

246

247

248

249

Figure 2 Schematic illustrating some of the key components of identifying objects using MODE. (a) Defining some of the terminology and key components for computing matched pairs. (b) Example of how the best matched pair is identified.

250 The important steps for applying MODE can be summarised as follows (which are described in detail in
251 Davis et al. 2006):

- 252 1) Both forecast and observation (or analysis) need to be on the same grid. Typically, this means
253 interpolating the observations to the model grid to avoid the model being expected to resolve
254 features which are sub-grid scale.
- 255 2) Depending on how noisy the fields are they should be smoothed. ~~It is worth remembering that~~
256 the Gridded observations (not analyses) can be noisy and usually need some smoothing. Models
257 and model analyses are built on numerical methods which come with discretisation effects.
258 Depending on the method this implies that any model's true resolution (i.e. the scales which the
259 model is resolving) is between 2 and 4 times the horizontal grid (mesh) resolution. The number
260 of objects identified will vary inversely with the smoothing radius.
- 261 3) Define a threshold which captures the feature of interest and apply it to both the smoothed
262 forecast and observed fields to identify simple objects as shown in Figure 2.
- 263 4) Any smoothing is only for object identification purposes. The original intensity information
264 within the object boundaries is analysed.
- 265 5) Lastly, the object matching is accomplished using a fuzzy logic engine (low level artificial
266 intelligence), which is expressed as the so-called "interest" score as shown in Figure 2(b). The
267 higher the score the stronger the match. All objects are compared in both fields and interest
268 scores are computed for all combinations. A threshold is set on the interest score value (typically
269 0.7) to denote which are the best matches, and on the unique pairing with the highest score is
270 kept for analysis purposes. Some objects will remain unmatched (either because there is none or
271 because there are no interest values above the set threshold to provide a credible match) and
272 these can be analysed separately.

273 MODE is highly configurable. To gain an optimal combination of configurable parameters for each
274 application requires extensive sensitivity testing to gain sufficient understanding of the behaviour of the
275 data sets to be examined, and to achieve, on average, heuristically the right outcome. Initial tuning
276 requires user input to check whether the method is replicating what a human would do.

- 277 1) The sensitivity to threshold and smoothing radius should be explored. The threshold and
278 variability in the fields can affect the number of objects which are identified. The process of
279 exploring the relationship between threshold and smoothness helps to identify what would
280 heuristically be considered a reasonable number of objects.
- 281 2) The sensitivity to the merging option must also be investigated. In this instance the merging
282 option had very little impact.
- 283 3) The behaviour of the matching can also be configured, with a number of options ranging from
284 the simple to the more complicated, which added computational expense. There may be very
285 little difference in outcomes, but it is worth checking. Here the *merge_both* option was used but
286 it was not strictly necessary as there was little difference between the available options.

287

288 Note also that a minimum size (area) is set for object identification. This is often a somewhat pragmatic
289 choice. If the size is set too small, too many objects are identified, which end up being merged. If too
290 large, very few objects are identified. Here a minimum area of 10 grid squares ($\sim 70 \text{ km}^2$) was used for
291 an object to be included in the analysis. For this study the default settings were used for matching and
292 computing the interest score (as provided in the default configuration file (see example configuration
293 files in https://github.com/dtcenter/MET/tree/main_v8.1/met/scripts/config). The default threshold of
294 0.7 for the interest score was also used to identify acceptable matches.

295

296 Identical to MODE, identifying time-space objects in MTD uses smoothing and thresholding. Applying
297 a threshold yields a binary field where grid points exceeding the defined threshold are set to one. At this
298 stage each region of non-zero grid points in space and time is considered a separate object, and the grid
299 points within each object are assigned a unique object identifier. For MTD the search for contiguous
300 grid points not only means examining adjacent grid points in space, but also the grid points in the same
301 or similar location at adjacent times to define a space-time object. The same fuzzy logic-based
302 algorithms used for merging and matching in MODE apply to MTD as well. Similarly, to MODE a
303 minimum volume must be set. Here a volume threshold of 1000 grid squares (a summation of the daily
304 object areas identified to be part of the space-time object) was imposed for space-time object

305 identification to be included in the analysis. This represents the accumulated number of grid squares
306 associated with an object over consecutive time slices. Otherwise, the default settings were used for
307 object matching. For MTD a lower interest score of 0.5 was used for matching objects. Finally, it is
308 worth noting that the MODE and MTD tools, though similar, are completely independent of each other,
309 and were set up differently here. MODE is ideal for understanding the identified features in individual
310 daily fields in some detail. MTD, it was felt, would be best used to look at larger scales. Here it was set
311 up to capture the most significant (in size) and long-lasting blooms.

312

313 **3.2 Defining Chl-*a* concentration thresholds and other choices on tuneable parameters**

314 Chl-*a* can vary over several orders of magnitude. Often \log_{10} thresholds are used to match the fact that
315 Chl-*a* follows a lognormal distribution (e.g. Campbell 1995). Defining thresholds can be difficult: on
316 the one hand there is the desire to only capture events of interest, so the thresholds should not be too
317 low, whereas on the other hand if the thresholds are too high no events are captured and there is nothing
318 to analyse. From a regional (NW European Shelf) perspective the values of interest are typically in the
319 range of 3–5 mg m^{-3} (Schalles, 2006), though higher ~~values are present.~~Chl-*a* concentrations can be
320 measured in-situ or diagnosed in satellite products. For this study, the data sets were not transformed
321 but the thresholds were selected in such a way that they would correspond to set of being equally spaced
322 in logarithmic thresholds, ranging between 0.2 and 1.4 $\log_{10}\text{mg m}^{-3}$ were applied space, staying true to
323 the Chl-*a* fields, corresponding to underlying distribution shape of Chl-*a* concentrations between 1.62
324 and 25 mg m^{-3} . ~~Doing this removed the need to transform the data. In the paper.~~ Here the primary focus
325 is on the results for the 2.5 mg m^{-3} threshold, though some results for the 4 and 6.3 mg m^{-3} thresholds
326 are also presented.

327

328 In addition to the interpolation of the L4 ocean colour product onto the AMM7~7 km AMM7v11 grid, it
329 is important to ensure that MODE and MTD use optimal settings for the fields under study. Results are
330 sensitive to characteristics of the fields (how smooth or noisy). Right at the start the emphasis was on
331 finding the right combination of Chl-*a* concentration threshold and smoothing, balancing the need for
332 identifying objects with keeping the number of objects manageable. The guiding principles in

333 identifying the right combination were to ensure that the daily object count remained ~~less than 30~~low
334 enough, recalling that these methods were developed to mimic what a human would do. The human
335 brain would struggle to cope with as many as 30, but this was considered to be an acceptable upper limit
336 after considerable visual inspection of output. Furthermore, the smoothing applied needs to be reduced
337 with increasing concentration thresholds because objects become smaller and are less frequent. This is
338 to ensure that too much smoothing does not remove more intense objects from the analysis. However,
339 pushing the concentration threshold too high may also be ~~too~~-detrimental; depending on the input fields,
340 identified objects may be spurious ~~and too~~(due to e.g. a failure of quality control processes removing
341 such). Too few objects ~~will mean meaningful~~also make the compilation of robust aggregated statistics
342 ~~cannot be compiled. AMM7v11 analyses are on a ~7 km grid impossible.~~

343

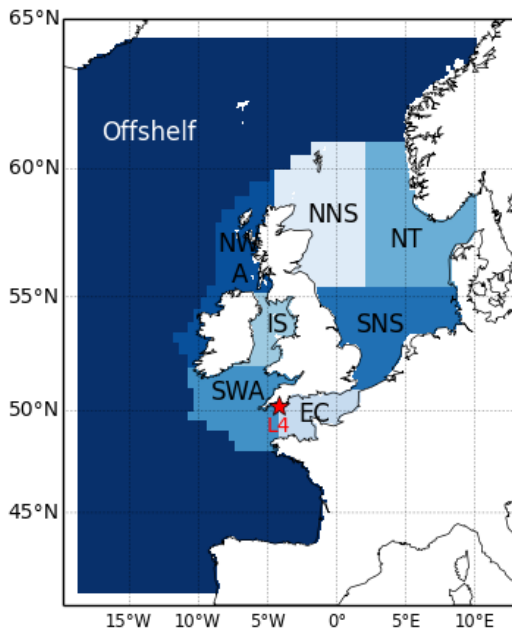
344 For the lowest thresholds including 2.5 and 4.0 mg m⁻³ a smoothing radius of 5 grid squares (~35 km)
345 was applied to both L4 and AMM7v11 fields, but for higher thresholds (e.g. 6.3 mg m⁻³) the smoothing
346 radius was reduced to 3 grid squares, to prevent the higher peak concentrations, which are often small in
347 spatial extent, from being lost due to the smoothing. Thresholds above 6.3 mg m⁻³ yielded too few
348 objects to be analysed with any rigour. The smoothing was particularly necessary for the L4 product
349 which, because of its native 1 km resolution is able to resolve very small (noisy) objects typically found
350 near the coast and which a 7 km resolution model cannot resolve. For the MTD analysis, objects in the
351 L4 ocean colour product and the AMM7v11 analyses were only defined using a Chl-*a* concentration
352 threshold of 2.5 mg m⁻³.

353

354 4. Results

355 4.14.1 Traditional statistics

356 Traditional verification metrics are based on a set of observations and a set of model outputs matched in
357 time and space. The statistics that are typically considered (McEwan et al., 2021) are the median error
358 (bias), median absolute difference (MAD) and Spearman rank correlation coefficient. The median bias
359 gives indication of consistent differences between the model and observations, with a positive bias
360 indicating the model concentration is higher than observed. The MAD provides an absolute magnitude
361 of the difference. The Spearman rank correlation coefficient is the Pearson correlation coefficient
362 between the ranked values of the model and observation data so that if the model data increases when
363 the observations do, they are positively correlated. It has the same interpretation as the more common
364 Pearson correlation coefficient where a correlation of 1 shows perfect correlation and 0 shows no
365 correlation. Error! Reference source not found. provides a map of the model domain and the
366 subregions over which traditional metrics are computed. Table 1 shows results for log(Chl-*a*) assessed
367 against the L4 ocean colour product.



Regions:

EC: English Channel

IS: Irish Sea

NNS: Northern North Sea

NT: Norwegian Trench

NWA: North Western Approaches

SNS: Southern North Sea

SWA: South Western Approaches

The Continental Shelf regions includes all the above, i.e. all regions except Off-shelf.

Observation stations:

L4: station L4 of the Western Channel Observatory

368

369

Figure 3 Map showing the sub-regions over which statistics are computed.

370

371 **Table 1 Statistics for matched pairs of daily model surface log-chlorophyll-*a* outputs and satellite ocean colour Chl-*a***
 372 **for the full domain and sub-regions for the period March to July 2019. See Error! Reference source not found. for the**
 373 **location of the regions. The Continental shelf includes all regions except Off-shelf (ICES, 2014)**

<i>Region</i>	<i>Median bias (log(mg m⁻³))</i>	<i>MAD (log(mg m⁻³))</i>	<i>Spearman correlation coefficient</i>
Full Domain	<0.01 (0.004)	0.21	0.62
Continental shelf	-0.09	0.17	0.71
Off-shelf	0.06	0.23	0.51
Norwegian Trench	-0.04	0.18	0.61
Northern North Sea	-0.05	0.17	0.64
Southern North Sea	-0.17	0.19	0.82
English Channel	-0.13	0.16	0.68
Irish Sea	-0.13	0.19	0.49
South Western Approaches	-0.07	0.15	0.69
North Western Approaches	<0.01 (0.006)	0.18	0.51

374

375 Compared with the L4 product, the AMM7v11 analysis slightly overestimates Chl-*a* off-shelf, and
 376 underestimates Chl-*a* in the on-shelf regions (Table 1). Regions show moderate to strong positive
 377 correlations, highest in the Southern North Sea and lowest in the Irish Sea. These statistics give useful
 378 insight into model skill but provide limited information about how model performance changes as the
 379 bloom season progresses (McEwan et al., 2021; Skákala et al., 2018, 2020). As will be shown, the
 380 output from MODE and MTD provides a very different perspective from these traditional verification
 381 metrics, allowing a more detailed understanding of model performance.

382

383 **4.2 Chl-*a* distributions**

384 It is important to understand the nature of the underlying L4 and AMM7v11 Chl-*a* distributions and any
 385 differences between them. This can be done by creating cumulative distribution functions (CDF) of the
 386 log₁₀ L4 and AMM7v11 Chl-*a* concentrations, by taking all grid points in the domain and all dates in
 387 the study period. These are plotted in Figure 4, showing that there is an offset between the distributions,

388 the AMM7v11 analysis having more low concentrations, though the distributions appear to be
389 converging in the upper tail.

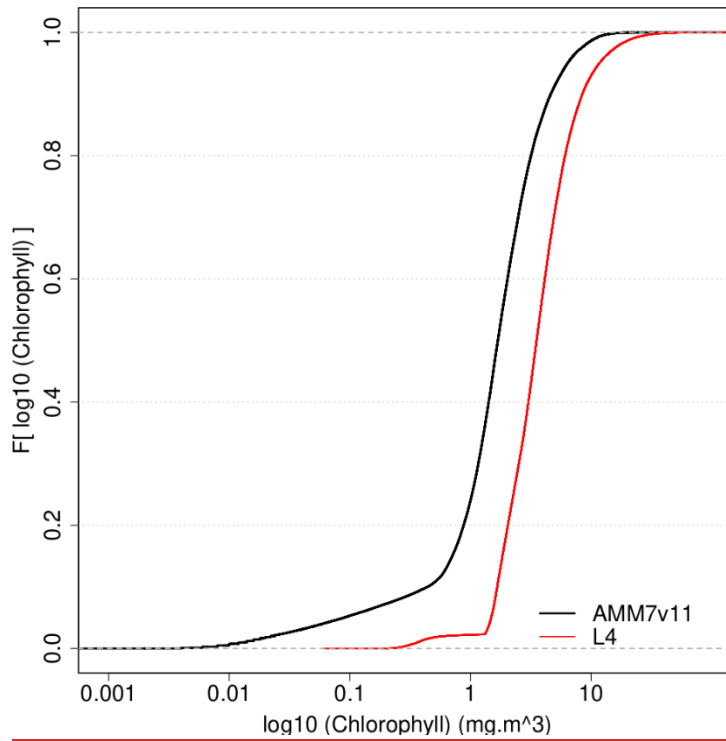
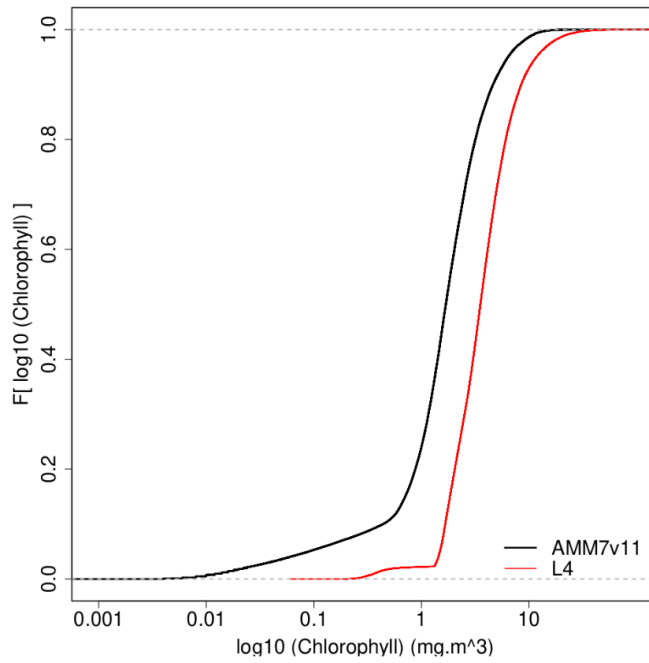
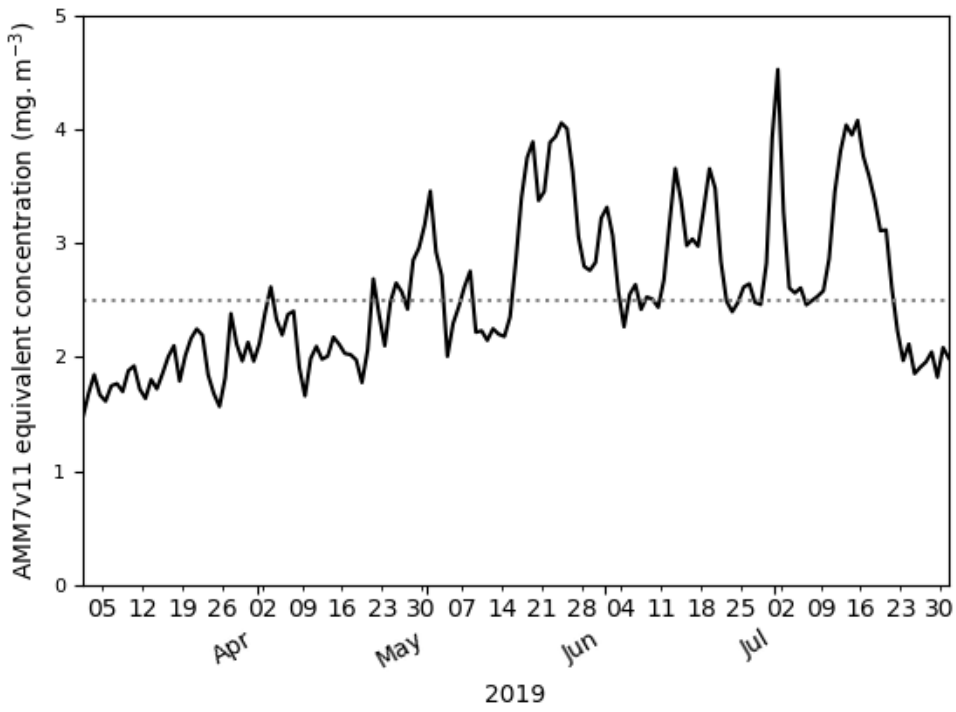
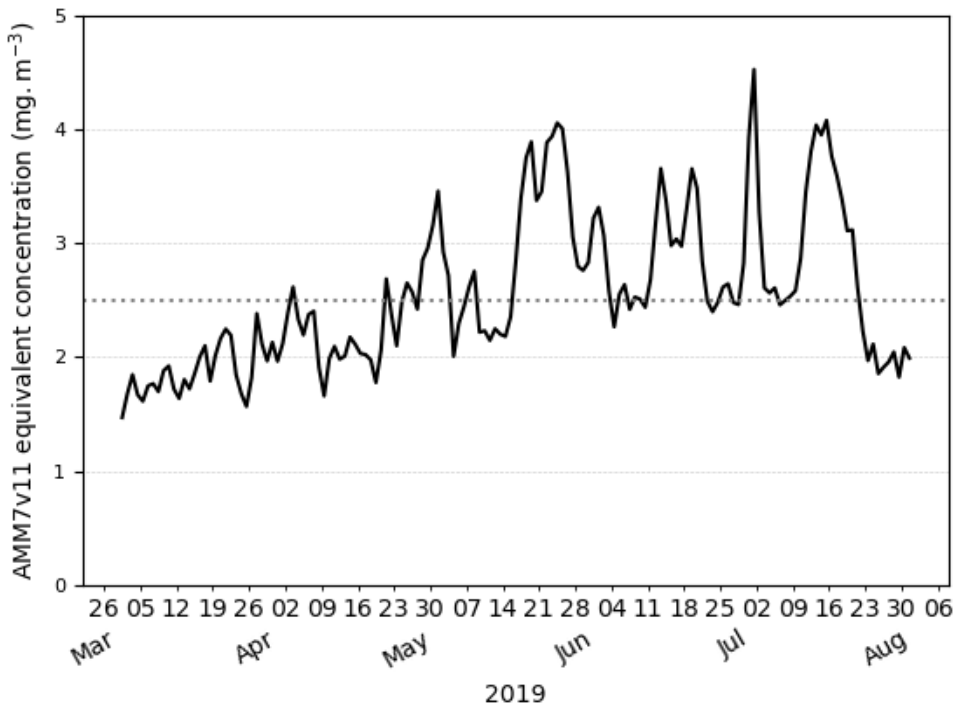


Figure 4 Empirical cumulative distribution functions of the log₁₀ Chl-a concentration for the L4 ocean colour product and AMM7v11 analyses for the 2019 bloom season.

394 Exploring this further the AMM7v11 and L4 Chl-*a* concentration CDFs can be derived for each
395 individual day, rather than for the season as a whole. From these the ~~eentilequantile~~ where the L4
396 product is less than or equal to 2.5 mg m^{-3} (29.7%) can be compared to the corresponding AMM7v11
397 ~~eentile value.concentration associated with the same quantile of 29.7%. From~~ Figure 4 this gives an
398 equivalent concentration of 1.15 mg m^{-3} for the season. The daily matched ~~eentilequantile~~ Chl-*a* values
399 provide an estimate of the daily bias. This is plotted in Figure 5 as a time series for the 2019 bloom
400 season. It shows that the daily AMM7v11 corresponding ~~eentilequantile~~ values are mainly in the range
401 of $\sim 1.5\text{--}4.5 \text{ mg m}^{-3}$, averaging out to 2.9 mg m^{-3} over the season, which suggests a modest difference
402 overall. The larger day-to-day variations show some cyclical patterns. There are notable peaks at the
403 end of May and the beginning of July. An inspection of the fields (not shown) suggests that at these
404 times the AMM7v11 appears to have higher Chl-*a* concentrations over large portions of the domain
405 compared to the L4 product.



406



407

408 **Figure 5** The day-to-day AMM7v11 eentilequantile Chl-*a* value corresponding to the L4 product eentilequantile
409 representing 2.5 mg m^{-3} derived from the L4 daily CDFs. The mean AMM7v11 Chl-*a* equivalent eentilequantile value
410 for the 2019 season is 2.9 mg m^{-3} .

411

412 In employing a threshold-based approach, generally the same threshold is applied to both data sets. In
413 the presence of a bias this requires a little bit of thought. In extreme cases, it could mean the inability to
414 identify objects in one of the data sets, which would then mean objects cannot be matched and paired,
415 negating the purpose of a spatial method like MODE or MTD. Not being able to identify any objects
416 does provide some useful information, though arguably not enough context. The lack of objects does
417 suggest the presence of a bias but it does not provide any sense of whether the model is producing a
418 constant value of Chl-*a* for example, which would be of no use to the user, or whether it does capture
419 regions of enhanced Chl-*a*, albeit with an offset which means it does not exceed the set threshold.
420 Therefore, a more likely scenario is that a bias could partially mask relevant signals in the derived
421 object properties, which could lead to the potential misinterpretation of results. If there is a significant
422 risk of this occurring the bias could be addressed before features are identified to ensure that the
423 primary purpose of using a feature-based assessment can be achieved, i.e. identifying features of interest
424 in two sets of fields to assess their location, timing and other properties and assessing their skill. The
425 fact that there is an intensity offset should not prevent the method from providing information about the
426 skill of identified features. ~~In this instance, though there is bias, it did not prevent the identification of
427 objects in either fields to the extent where the results did not reflect the potential for the analyses to
428 provide features which could be matched, paired and compared.~~ As is seen here, though there is bias (as
429 seen in Figure 4Figure 5), it does not prevent the method from successfully identifying objects using the
430 same threshold for both datasets, though it will be shown that the effect of the bias can affect some
431 object attributes, e.g. object areas. However, a more prohibitive bias could compromise the methods,
432 e.g. being unable to identify objects in a dataset. This would have a disproportionate effect on the
433 statistics for the matched pairs in particular. Under such circumstances the quantile mapping
434 functionality within MODE (to remove the effect of the bias) is strongly recommended.

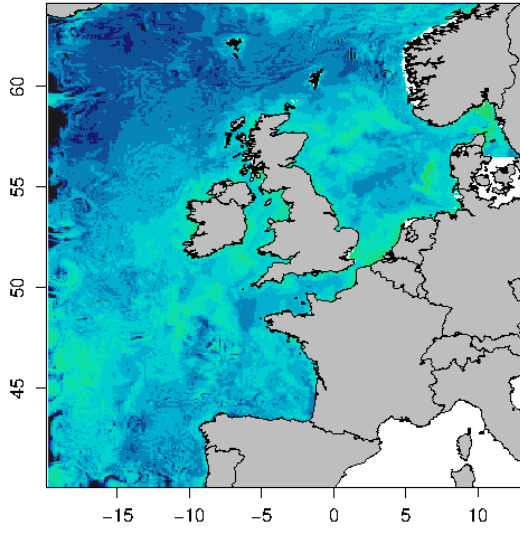
435 **4.23 Visualising daily objects**

436 Figure 6 shows the daily Chl-*a* concentration fields as represented in the L4 ocean colour product and
437 the AMM7v11 analyses for 21 April 2019, which is near the peak of the bloom season. The respective
438 fields are plotted in (a) and (b), noting that the 1 km resolution L4 product has been interpolated onto

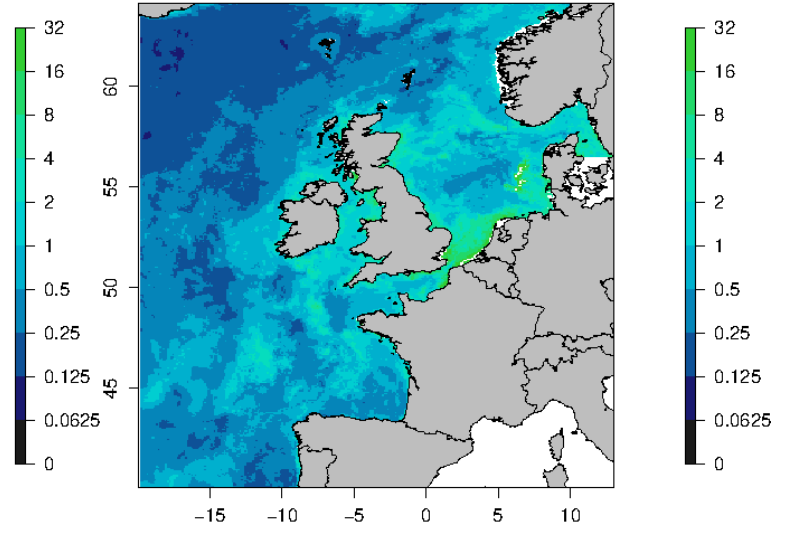
439 the ~7 km AMM7 grid. Applying a threshold of 6.3 mg m^{-3} to both with a smoothing radius of ~21 km
440 (3 grid lengths) yields 8 objects in the AMM7v11 analysis (7 visible in this zoomed region) and 11
441 objects in the L4 product. As discussed, the bias described in Section 4.1 does not appear to prevent the
442 identification of objects in the L4 product and the AMM7v11 analyses, and the process of finding
443 matches is possible.

444

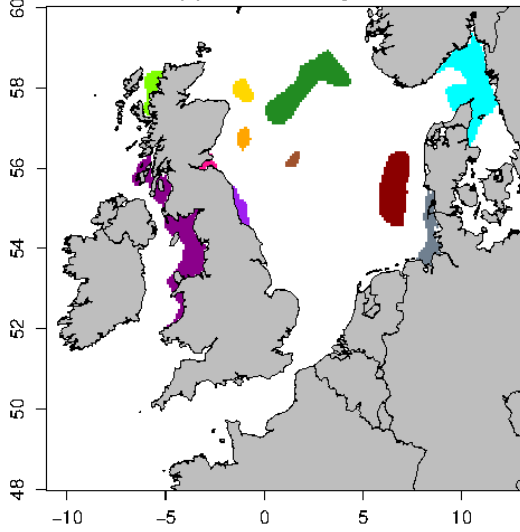
(a) AMM7v11 analysis



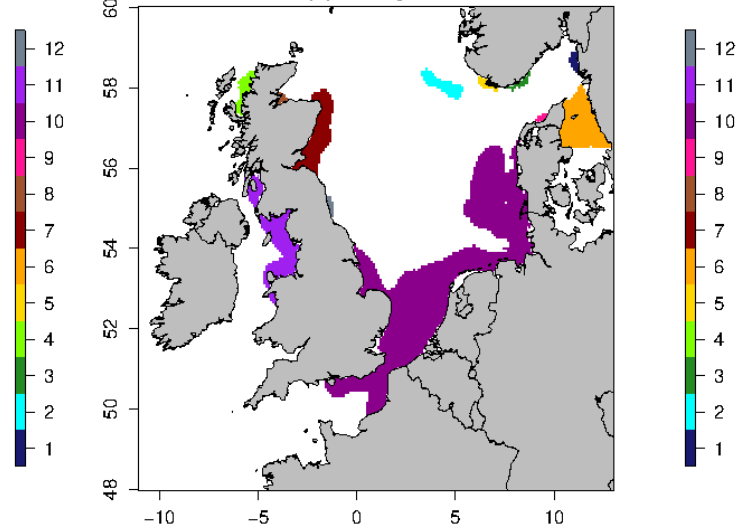
(b) L4 product



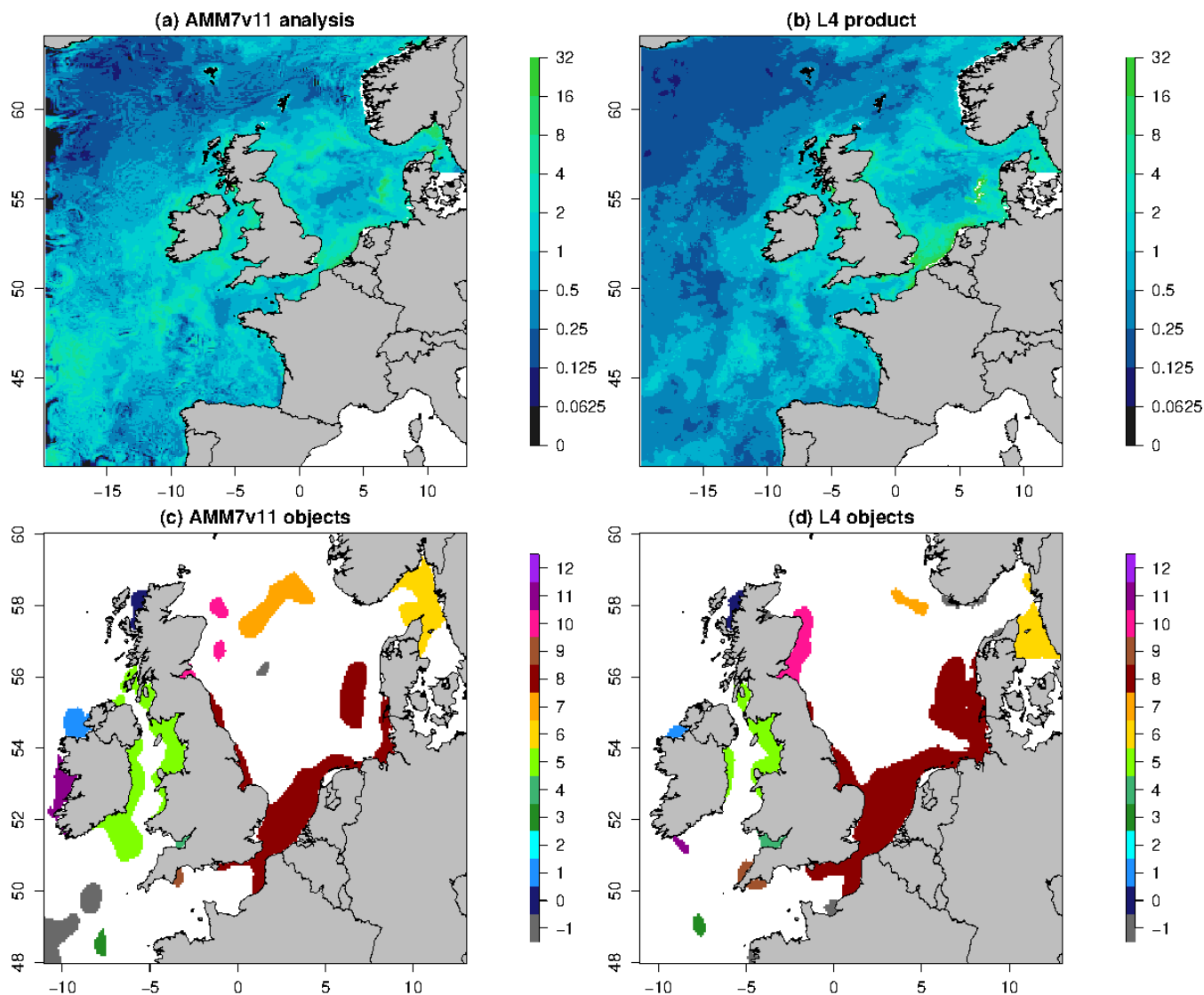
(c) AMM7v11 objects



(d) L4 objects



445



446
 447 **Figure 6** Daily Chl-*a* concentrations (in mg m^{-3}) for 21 April 2019: (a) AMM7v11 analysis and (b) L4 ocean colour
 448 product. The MODE objects shown in (c) and (d) are identified using a threshold of 6.3 mg m^{-3} and a smoothing
 449 radius of $\sim 21 \text{ km}$. The colour matches the object identification numberNote (c) and (d) show a smaller (inner)
 450 domain. The colours show the matching clusters. Objects denoted with -1 (grey) are unmatched.
 451

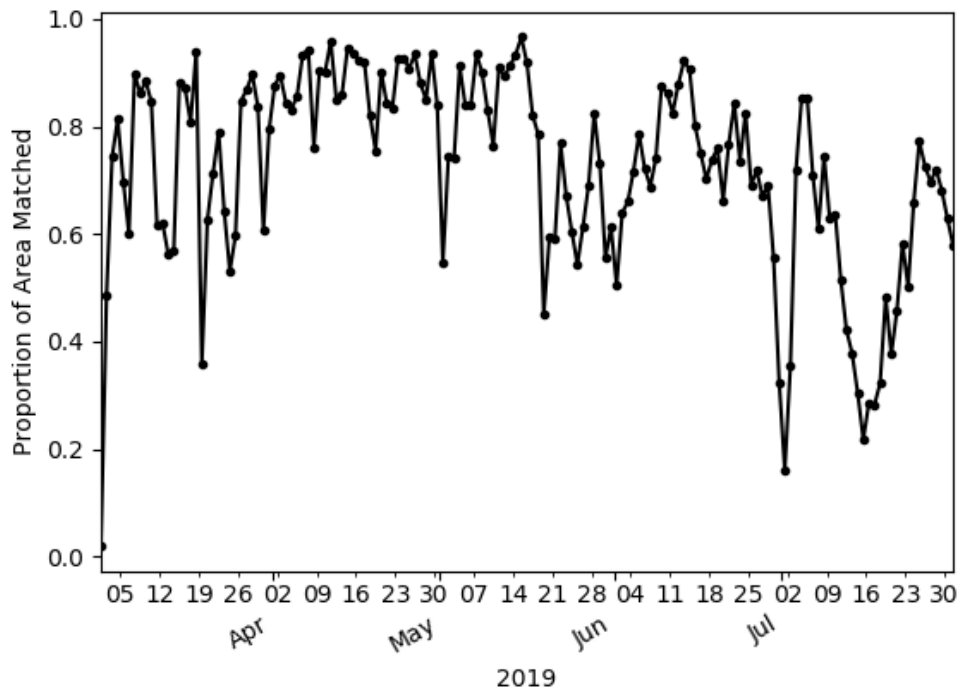
452 **4.34** Spatial characteristics

453 This section demonstrates the kinds of results that can be extracted from the two-dimensional MODE
 454 objects. Aspects of the marginal (AMM7v11 or L4 product only) and joint (matched/paired)

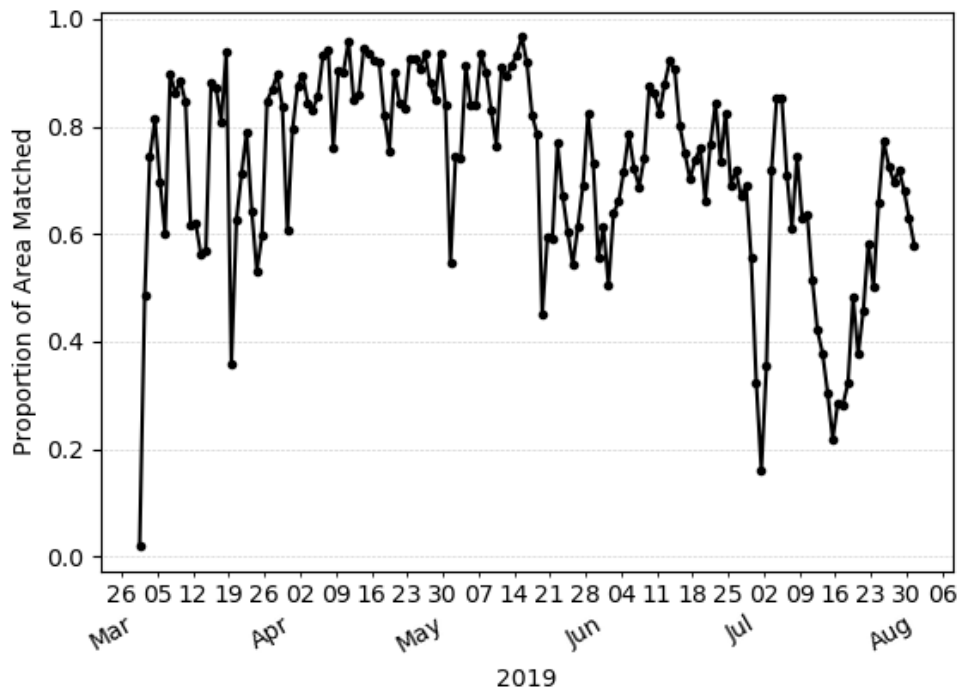
455 distributions can be examined. This includes object size (as a proxy for area) but also the proportion of
456 areas that are matched or unmatched.

457

458 Firstly, how similar is the L4 ocean colour product and the AMM7v11 analysis in terms of the features
459 of most interest, i.e. the Chl-*a* blooms? Figure 7 shows the evolution of the proportion of matched
460 object areas (to total combined area) through the 2019 season, when using MODE to compare the L4
461 product and AMM7v11 analyses, to further explore the differences (and similarities) between them. A
462 value of one would suggest that all identified areas are matched. Values less than one suggest that some
463 objects remain unmatched. The relatively high values of matched object-to-total area during April are
464 due to the large numbers of well-matched, physically small coastal objects in addition to the larger Chl-
465 *a* bloom originating in the Dover Straits (not shown). There is a notable minimum at the beginning of
466 July. Inspecting the MODE graphical output reveals this is in part due to only a few small objects being
467 identified, and this is compounded by their complete mismatch; the L4 objects are all coastal, whilst the
468 AMM7v11 objects are either coastal (but not in the same location as L4 objects) or in the deep waters of
469 the North Atlantic, to the north-west of Scotland. The relatively high proportions either side of this time
470 arise from a better correspondence in placement of the coastal objects (noting that there is a distance
471 limit on how far objects can be apart for the matching process to have a positive contribution to the
472 interest score).



473



474

475 **Figure 7 Proportion of total object area which is matched. Underlying matched and unmatched object areas (in units**
 476 **of numbers of grid squares) are taken from the MODE output. These areas are for the 2.5 mg m^{-3} concentration**
 477 **threshold objects.**

478

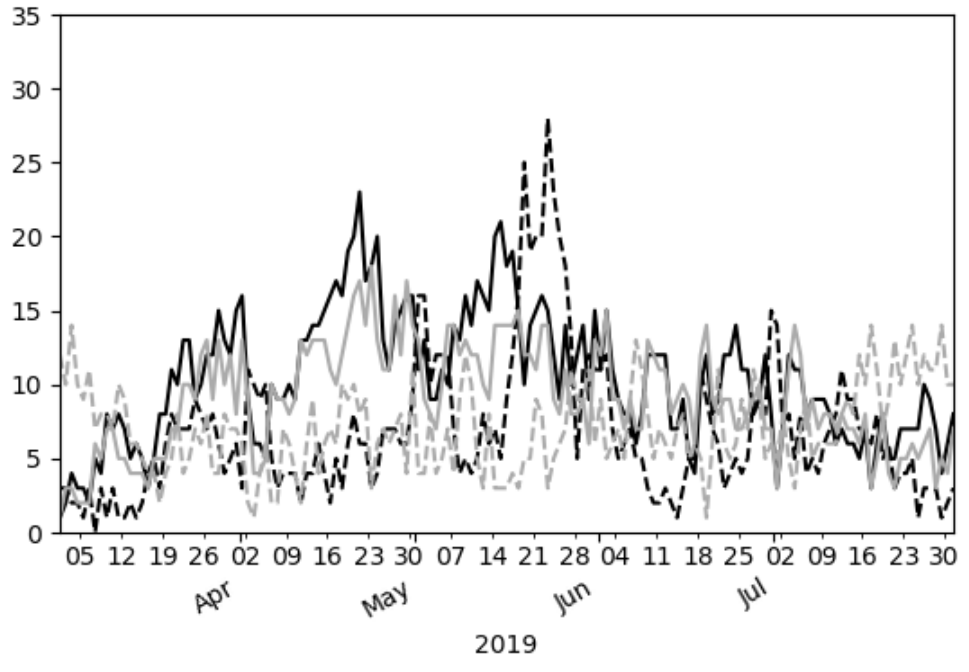
479 Overall, the AMM7v11 analysis is similar, but clearly not identical, to the L4 product. Best
480 correspondence appears to be during the first half of the bloom season. Later in the season the model's
481 determination to produce blooms in deep North Atlantic waters is a model deficiency that the
482 assimilation is (at this stage) unable to fix. The AMM7v11 analyses could conceivably be used as a
483 credible source for assessing the AMM7 Chl-*a* forecasts in the future. The major benefit of using a
484 model analysis is that it is at the same spatial resolution, with the same ability to resolve Chl-*a* bloom
485 objects, especially along the coast (i.e. the analysis limits the uncertainty due to whether an object could
486 be missing due to the inability of the model to resolve the feature).

487

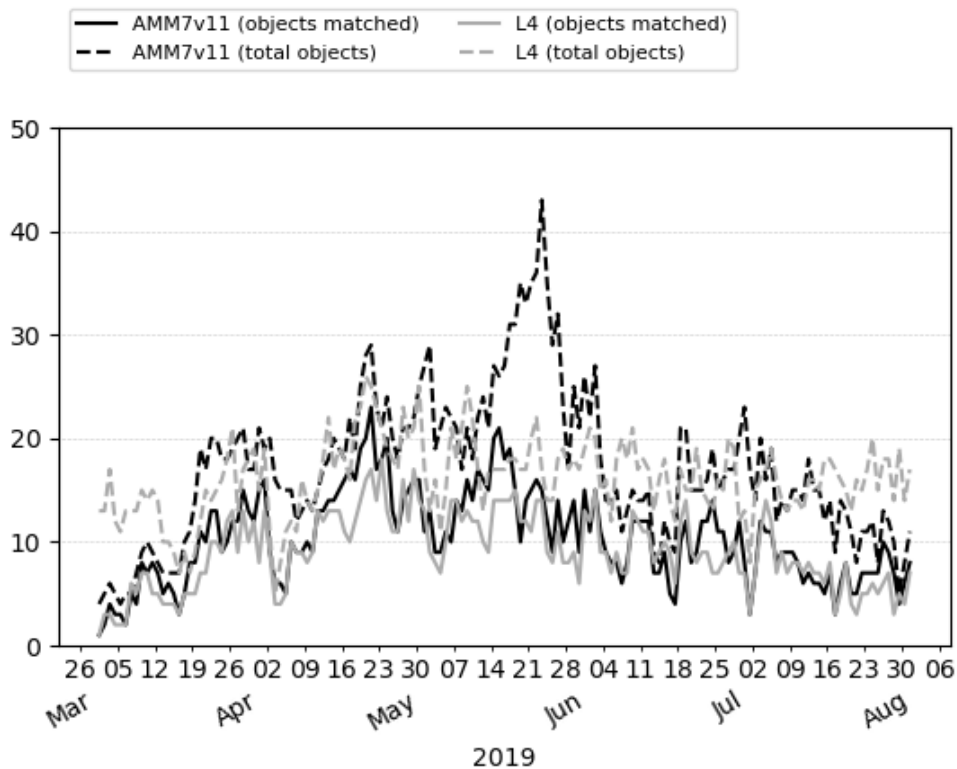
488 The day-to-day number of objects identified through the 2019 bloom season is shown in Figure 8^{obj},
489 illustrating how elements of the marginal and joint distribution ~~information~~ provided by MODE can be
490 used together. Here ~~both~~, numbers of total and matched (joint) ~~and unmatched (marginal)~~ objects are
491 shown. ~~From an interpretation perspective~~ If the AMM7v11 analyses are good (i.e. similar to the L4
492 product), there should be fewer unmatched (marginal) objects than matched ones (indicated by the
493 proximity of the solid and dashed lines); ideally there would be no unmatched objects in either the
494 forecastL4 product or the AMM7v11 analysis). In Figure 8 the number of objects in AMM7v11 starts
495 off small and increases as the bloom develops. For the L4 product there are already many objects
496 identified at the start of the timeseries, leading to many unmatched L4 objects- (these could be
497 considered misses in a more categorical analysis). A spike in the number of matched objects seen in
498 early April can be attributed to several coastal locations, which appear to be spatially well-matched. In
499 addition, a larger Chl-*a* bloom is seen in the Dover Straits region in the L4 product and although not
500 exactly spatially collocated, the objects are matched. There are a consistently large number of
501 unmatched objects seen in the AMM7v11 analysis and L4 ocean colour product from the end of May
502 onwards. In the AMM7v11 analysis this appears to be due to an increase in small objects identified,
503 mainly to the west, north and east of the United Kingdom. The increase in unmatched objects in the L4
504 ocean colour product is of a different origin, being due to an increase in localised coastal blooms.
505 Generally, the AMM7v11 analyses do not have the resolution to resolve these. Overall, there are 2632

506 AMM7v11 bloom objects identified in the season using the 2.5 mg m⁻³ threshold, and 2341 L4 bloom
507 objects, with 56% of AMM7v11 objects matched and 59% of L4 objects matched.

508 The identified objects in AMM7v11 and the L4 product can also be considered spatially over the season
509 by compositing the objects. This is done by counting the frequency with which a given grid square falls
510 within an identified object on any given day, essentially creating a binary map. These can be added up
511 over the entire season to produce a spatial composite object or temporal “frequency-of-occurrence” plot.



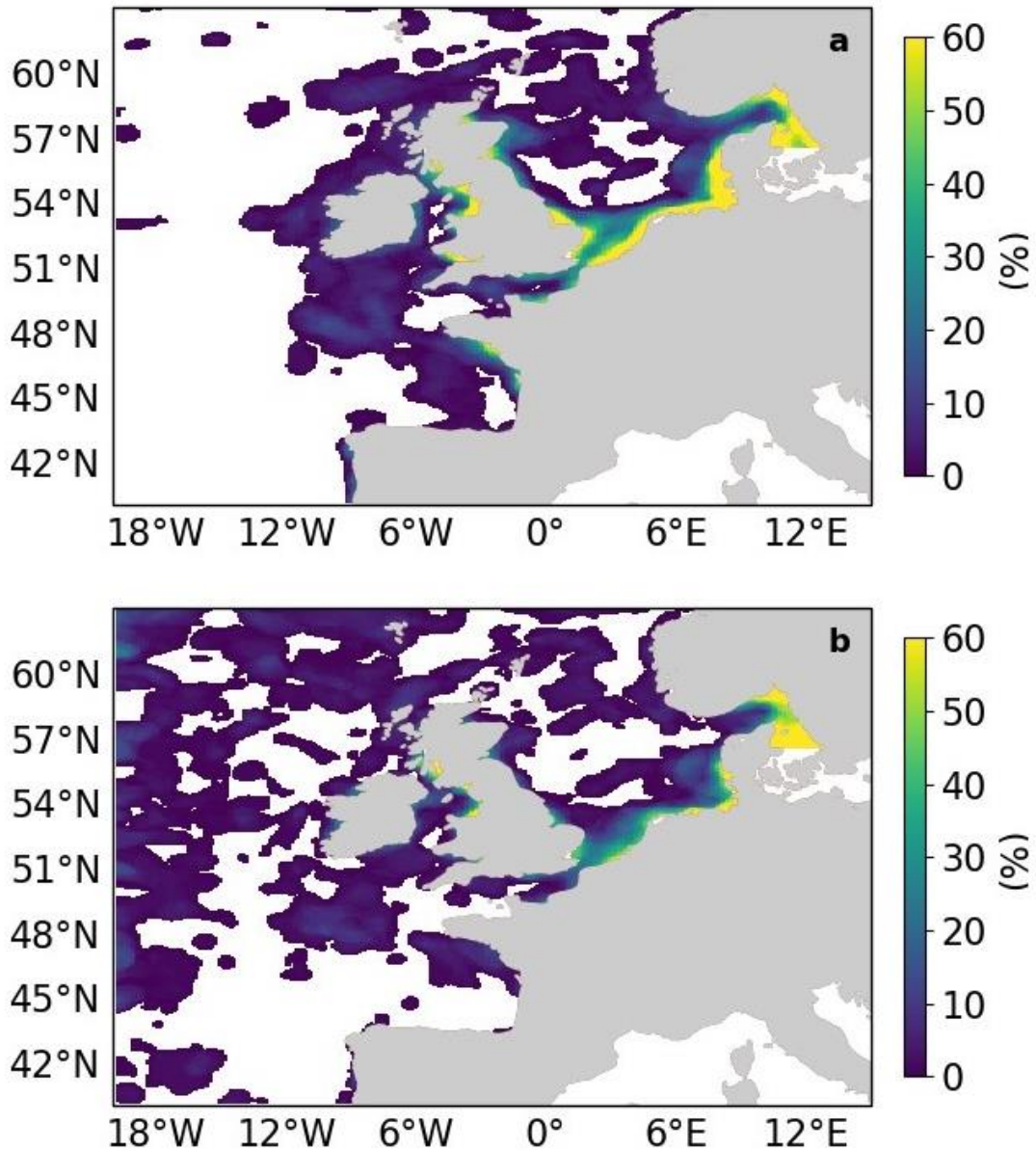
512



513

514 **Figure 8** Time series of the number of matched and ~~unmatched~~**total** objects **per day** from MODE comparing
 515 AMM7v11 analyses (black) with L4 satellite product (grey). Objects are identified using a threshold of 2.5 mg m⁻³.
 516 **Total object numbers for the season are 2341 for L4 satellite product and 2632 for AMM7v11.**

517 Figure 9 shows this spatial composite for the 2019 bloom season for the L4 ocean colour product
 518 objects (a) and the AMM7v11 objects (b). These are the composites based on the 2.5 mg m⁻³ threshold
 519 objects. There are areas, for example in the South West Approaches, (SWA, see **Error! Reference**
 520 **source not found.**), where there appears to be a good level of consistency. AMM7v11 analyses have
 521 elevated Chl-*a* values along the northern and western edges of the domain, for a low proportion of the
 522 time, which are not seen in the L4 product. This is likely due to the way that nutrient and phytoplankton
 523 boundary conditions are specified in AMM7v11. Overall, the low temporal frequency extent of the
 524 AMM7v11 objects is greater than for the L4 product.

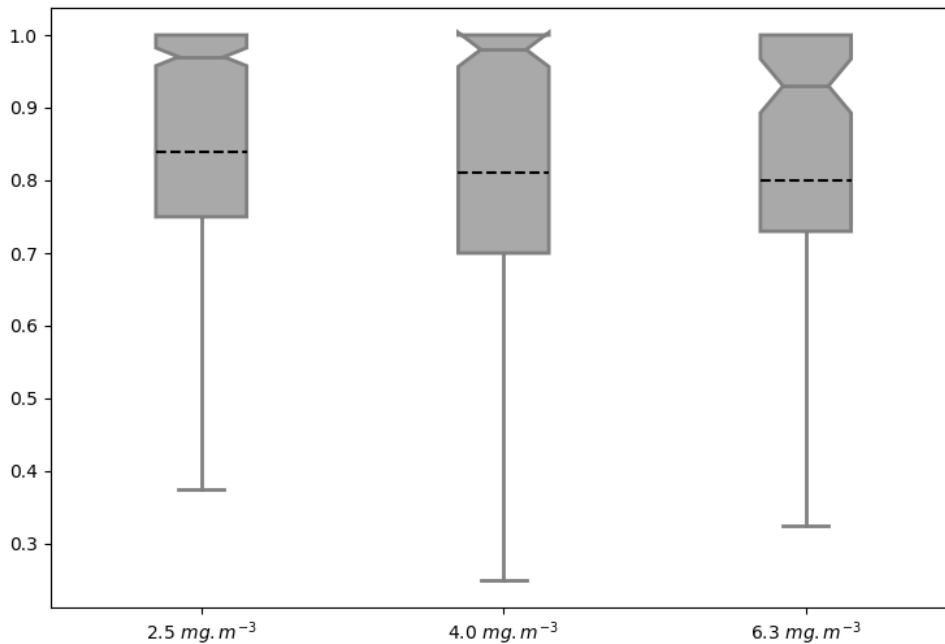


525

526 **Figure 9 Object composites (the proportion of time for which an object was present at the grid box throughout the**
 527 **2019 bloom season) for (a) the L4 ocean colour product objects and (b) the AMM7v11 analysis objects.**

528 Thus far all the attributes have been based on only the AMM7v11 or L4 objects. The distribution of
 529 object properties, derived for the season from the daily comparisons, can be summarised using box-and-
 530 whisker plots. Recall that the box encompasses the inter-quartile range (IQR, 25th to 75th

531 percentilequantile) and the notch and line through the box denotes the median or 50th percentilequantile.
532 The dashed line represents the mean, and the whiskers show ± 1.5 times the IQR. For clarity, values
533 outside that range have been filtered out of the plots shown here. Figure 10 shows the intersection-over-
534 area paired object attribute distribution as box-and-whisker plots for all object pairs during the 2019
535 bloom season, comparing the AMM7v11 analyses to L4 for three of the thresholds: 2.5 and 4.0 and 6.3
536 mg m^{-3} . The intersection-over-area diagnostic gives a measure of how much the matched (paired)
537 objects overlap in space. If the objects do not intersect, this metric is 0. The ratio is bounded at 1
538 because any area of overlap is always divided by the larger of the two object areas. The IQR for the 2.5
539 mg m^{-3} threshold is 0.25 with 50% of paired objects having an intersection-over-area of 0.97 or greater.
540 However, the lower whisker spans a large range of values to as low as 0.375, suggesting that there is a
541 proportion of object pairs with only small overlaps. There is quite a difference between the median
542 (notch) and the mean (dashed line) for this metric, suggesting the distribution is skewed with the mean
543 affected more by many small overlaps. For the 4.0 mg m^{-3} threshold paired objects the intersection-
544 over-area distribution is much broader, though the difference between the mean and medians is similar.
545 The proportion of paired objects with smaller overlaps has also increased. This should not be surprising
546 given that the objects generally get smaller with increasing threshold such that the ability for object
547 pairs to overlap actually decreases unless they are very closely collocated. At the 6.3 mg m^{-3} threshold
548 the median is lower (0.93) with a similar difference from the mean, however the sample size is much
549 smaller (only 130 paired objects over the season).



550

551 **Figure 10** Box-and-whisker plots of the paired object property “intersection area” ratio computed by dividing the spatially
 552 collocated area between the paired objects by the largest of either the AMM7v11 or L4 observed object areas (to keep the ratio to
 553 be bounded by 0 and 1). Three object thresholds are shown: 2.5 mg.m^{-3} , 4.0 mg.m^{-3} and 6.3 mg.m^{-3} . Smoothing radii of 5, 5 and 3
 554 grid lengths were applied for the three thresholds respectively. The sample sizes for each threshold were 1004, 401 and 130 paired
 555 objects respectively.

556

557 **4.45** Incorporating the time dimension

558

559 Having information in space *and* time enables one to ask, and hopefully answer questions such as: “*did*
 560 *the model predict the bloom to start in the observed location?*” or “*did the model predict the onset at*
 561 *the right time?*” and “*did the model predict the peak (in terms of extent) and duration of the bloom*
 562 *correctly?*”.

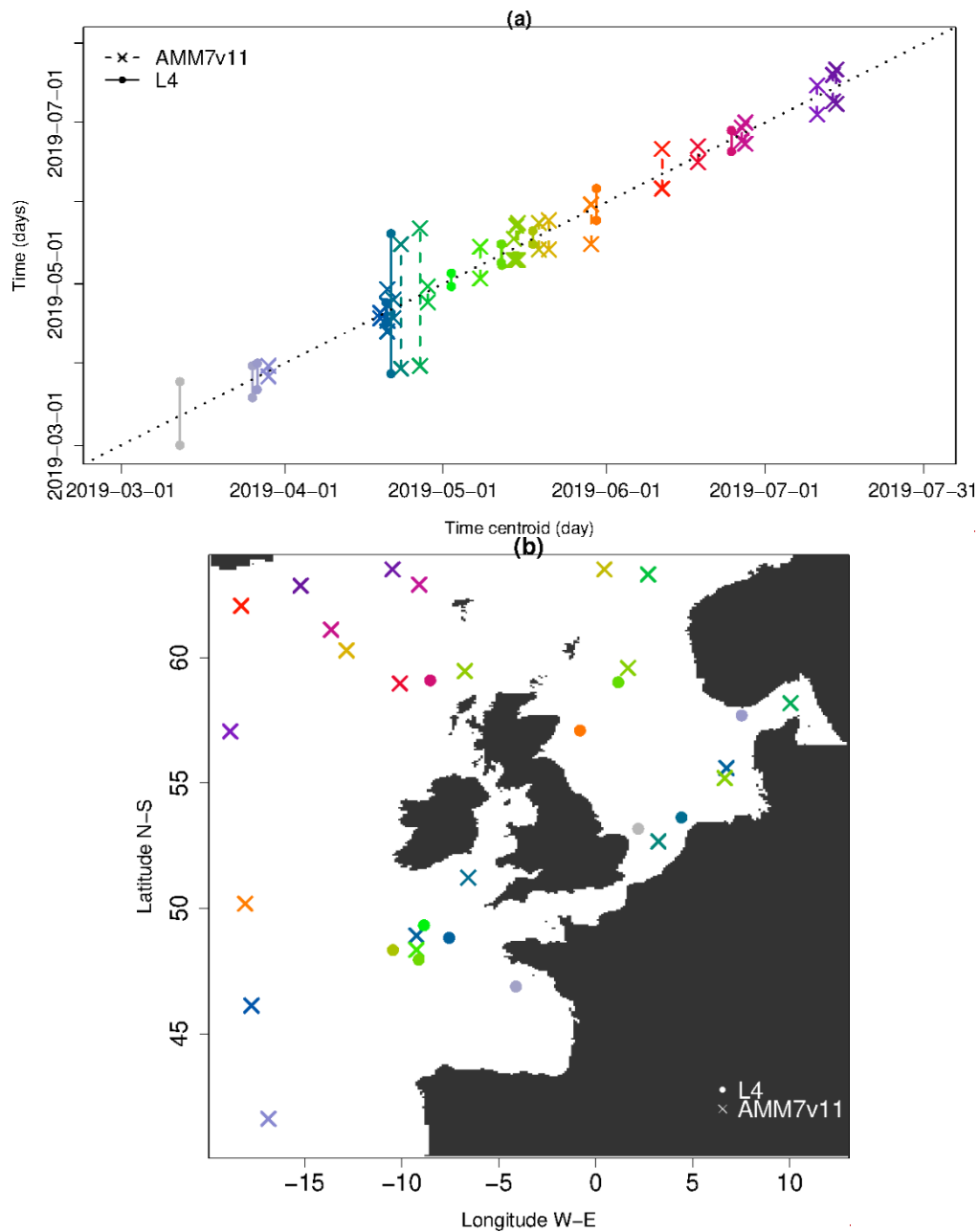
563

564 MTD identifies objects in space and time. As previously described, all MTD results are based on a 2.5
 565 mg.m^{-3} threshold applied to both the L4 ocean colour products and AMM7v11 analyses. A time
 566 centroid is derived from a time series of the spatial (two-dimensional) centroids which are computed for
 567 each (daily) time slice. In addition to this, each identified MTD object has a start and end time, and a

568 geographical location of the time centroid, which is the average of the two-dimensional locations. The
569 time component of the time centroid is weighted by volume.

570

571 The temporal progression of the 2019 bloom season along with spatial information as defined by the
572 MTD objects' is shown in . The object start and end times as well as the date of their time centroids ~~is~~
573 ~~shown in Figure 10, providing in (a) provide~~ a clear view of the onset and demise of each object (bloom
574 episode). In total there are 22 AMM7v11 and 11 L4 MTD objects. The x-axis in (a) represents elapsed
575 time. The location of the vertical lines along the x-axis on any given date indicates the date of the time
576 centroid whilst the duration of the space-time object can be gleaned from the y-axis based on the start
577 and end of the vertical line which defines the time the object was in existence. Solid lines represent the
578 L4 product objects whereas dashed lines represent the AMM7v11 objects. The colour palette is
579 graduated from grey and blue through green, yellow, red, and purple, denoting the relative time in the
580 season. In (a) the first Chl-*a* bloom object in the AMM7v11 analysis was identified on 29 March 2019
581 whereas in the L4 ocean colour product ~~this~~ the first bloom object was identified on 3 March, 26 days
582 earlier. The first time the L4 product and AMM7v11 analyses have concurrent objects (blooms) is in
583 late March. The L4 product also suggests that the season ends 30 June whereas the AMM7v11 analyses
584 persists the bloom season with objects identified until 23 July. Most AMM7v11 objects are of relatively
585 short duration, but overall, most groups of AMM7v11 objects have some temporal association with an
586 L4 product object around the same time, ~~though this does not mean they are geographically close to~~
587 ~~each other. This is illustrated in Figure 10(b) which provides the spatial context to (a). The colours and~~
588 ~~symbols are consistent for (a) and (b) and show that even when the MTD objects are identified at the~~
589 ~~same time they may be geographically quite far apart, or more typically there is no L4 counterpart~~
590 ~~(filled circle) to an AMM7v11 bloom object (cross). The north and westward progression of the bloom~~
591 ~~as the season unfolds can be seen through the use of the colours, with the AMM7v11 analysis producing~~
592 ~~many more objects in deeper waters to the north and west of the domain.~~

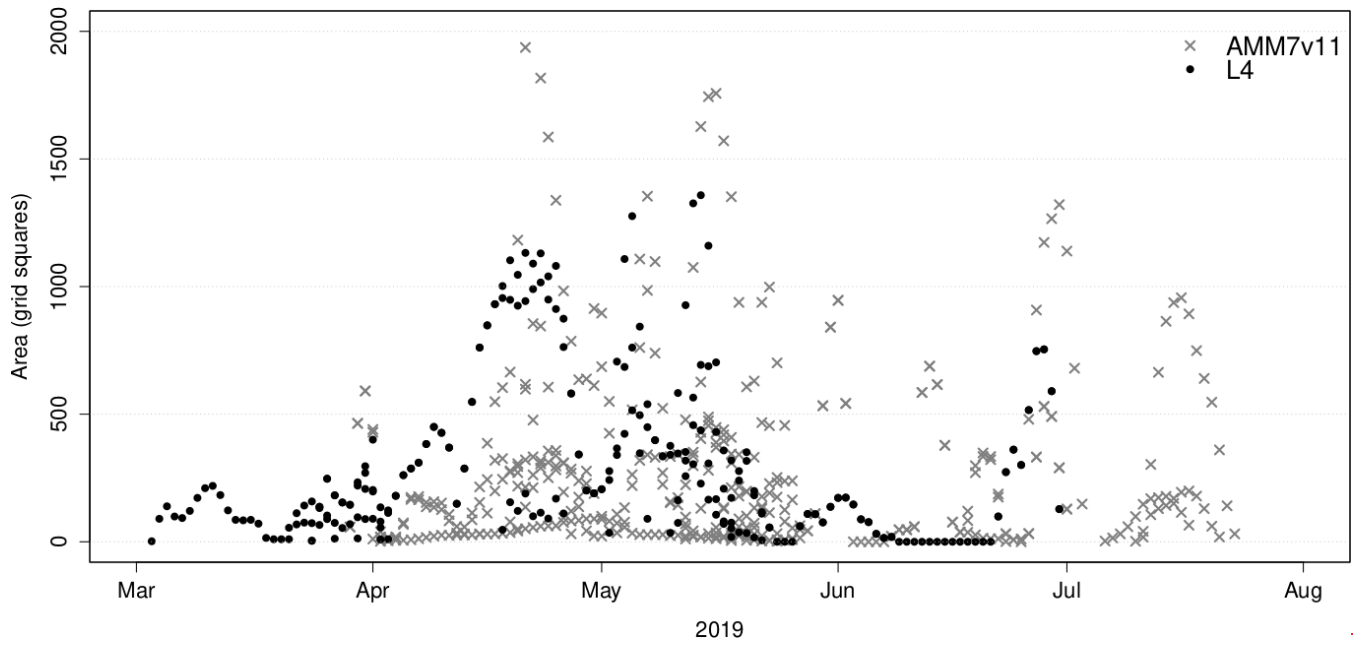


593

594

595 **Figure 10 Space-time information from the L4 (filled circle) and AMM7v11 (cross) MTD objects. (a) The timing of**
 596 **each identified bloom event (time centroid) plotted on the x-axis against the duration of the bloom event, denoted by**
 597 **the vertical line which represents the start and end time of each space-time object. The colours provide the ability to**
 598 **track the relative location within the 2019 season. (b) Spatial location of the time centroid shown in (a) to indicate**
 599 **that even if AMM7v11 and L4 objects exist at the same time they may not be geographically close. Colours are**
 600 **coordinated between (a) and (b).**

601
602 . In this instance it is also illuminating to consider a time series of all identifiedthe daily object areas
603 associated with the MTD objects (which are used to compute the volume of MTD objects). These are
604 plotted in Figure 11(b) showing all daily L4 object areas in ~~black~~the filled circles, and the AMM7v11
605 object areas ~~in grey (crosses-), in the same colours as in (a).~~ The main purpose is to highlight the
606 relative size of the L4 and AMM7v11 objects on any given day, as well as how many objects there
607 were. Recall that these are the objects identified using a Chl-*a* concentration threshold of 2.5 mg m⁻³.
608 Some of the AMM7v11 objects are considerably larger than those in L4 ~~though~~ in the middle~~mid- and~~
609 latter part of the bloom season ~~between~~from mid-May ~~and end June there is reasonable correspondence~~
610 ~~in identifying the peak in terms of extent and activity~~onwards, just not necessarily at exactly the same
611 time or location. ~~Of course, the AMM7v11 areas may also be larger because of the difference in the~~
612 ~~distributions noted in Figure 3, one of the reasons an awareness of the presence of any biases is~~
613 ~~important when interpreting results.~~ As seen in ~~Figure 10~~(b), the area time series also illustrates the
614 offsets in the start and end of the bloom season. Some of the objects detected in AMM7v11 beyond the
615 end of the observed bloom season provided by L4, suggests that at least three substantial areas are still
616 diagnosed to exceed the threshold of 2.5 mg m⁻³ into July. Taking the start of the earliest space-time
617 object as the onset of the bloom season and the end of the last object as the end, the 2019 season is 119
618 days long based on the L4 product, and 117 days in the AMM7v11 analysis. Therefore, the overall
619 length of the season as defined by the space-time objects is comparable in the AMM7v11 analysis,
620 albeit with a substantial offset. Finally, even if (a) and (b) suggest that AMM7v11 and L4 objects exist
621 at the nearly the same time, this does not mean they are geographically close to each other. This is
622 illustrated in (c) which provides the spatial context. The colours and symbols are consistent across all
623 panels and show that even when the MTD objects are identified at the same time they may be
624 geographically quite far apart, or more typically there is no L4 counterpart (filled circle) to an
625 AMM7v11 bloom object (cross). The north- and westward progression of the bloom as the season
626 unfolds can be seen through the use of the colours, with the AMM7v11 analysis producing enhanced
627 Chl-*a* concentrations in deeper waters to the north and west of the domain beyond the end of the
628 observed season.



629
630
631

Figure 11 Time series of all identified single simple MTD object areas in the AMM7v11 analysis and the L4 ocean colour product.

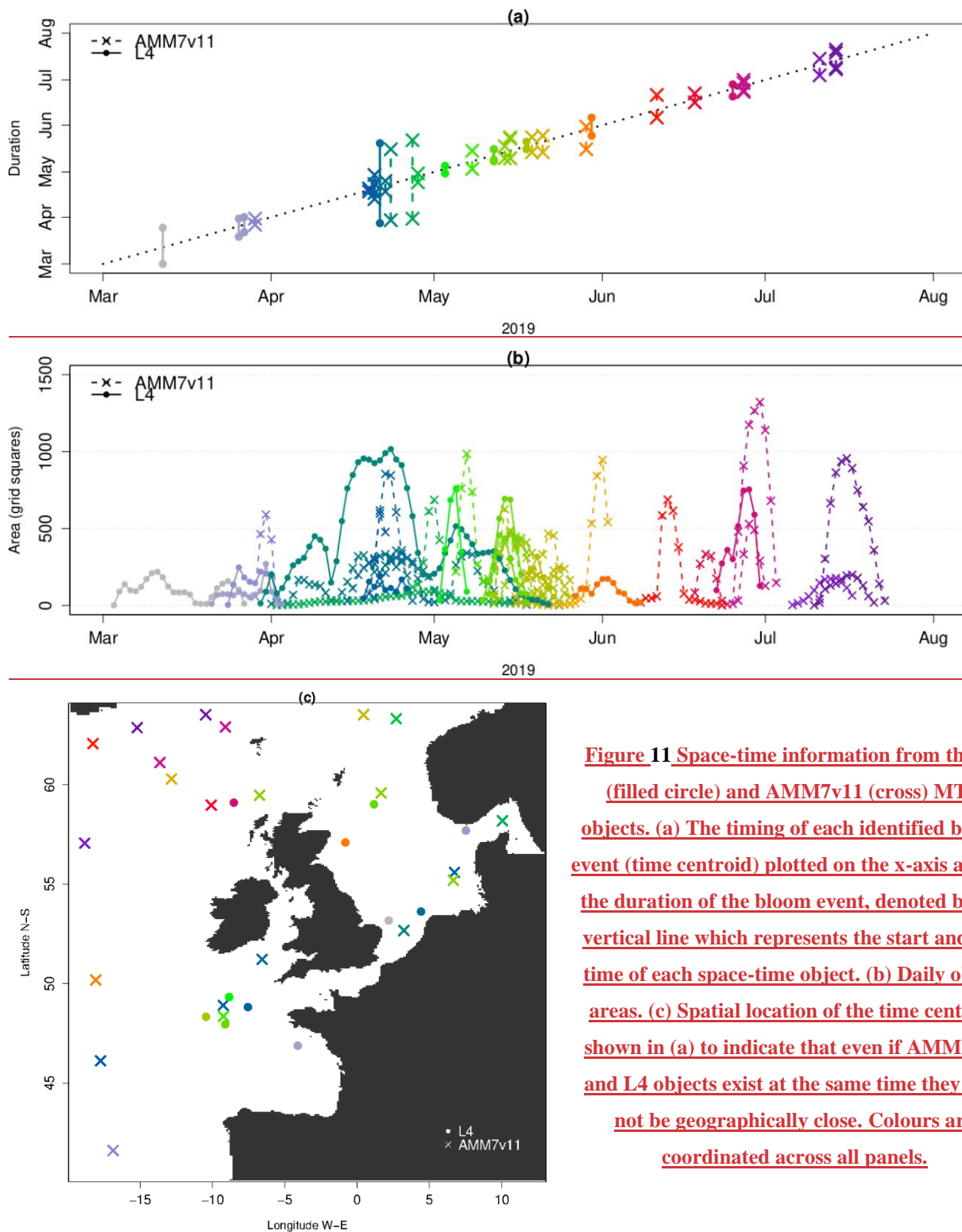


Figure 11 Space-time information from the L4 (filled circle) and AMM7v11 (cross) MTD objects. (a) The timing of each identified bloom event (time centroid) plotted on the x-axis against the duration of the bloom event, denoted by the vertical line which represents the start and end time of each space-time object. (b) Daily object areas. (c) Spatial location of the time centroid shown in (a) to indicate that even if AMM7v11 and L4 objects exist at the same time they may not be geographically close. Colours are coordinated across all panels.

632 With only 22 AMM7v11 and 11 L4 product MTD objects, which are temporally and geographically
633 well dispersed, three of the L4 objects remained unmatched, leaving only 8 matched MTD objects for
634 the 2019 bloom season with an overall interest score greater than 0.5. This represented an insufficient
635 sample for drawing any robust statistical conclusions. Nevertheless, some inspection of the paired MTD
636 object attributes are summarised below:

- 637 • The spatial centroid (centre of mass) differences can be extensive, but the majority are within 0 to
638 100 grid squares apart (i.e. up to ~700 km).
- 639 • The majority of paired objects have time centroid differences +/- 10 days.
- 640 • Considering the volumes of the space-time objects, half the paired objects have volume ratios of less
641 than 1, i.e. AMM7v11 objects tend to be smaller or similar in size. The other pairs have ratios as
642 high as 4.
- 643 • Overlaps between AMM7v11 and L4 MTD objects remain small and infrequent with only one pair
644 with a significant overlap in space and time.

645 **5. Discussion and conclusions**

646 MODE and MTD were used as two distinct but related feature-based diagnostic verification methods to
647 evaluate and compare the pre-operational AMM7v11 European North West Shelf Chl-*a* concentration
648 bloom objects to those identified in the satellite-based L4 ocean colour product. Nominally blooms were
649 said to occur when the concentration threshold exceeded 2.5 mg m⁻³ and two higher thresholds were
650 also considered. Sample sizes dwindle rapidly with increasing threshold. Of specific interest were the
651 similarities and differences in respective bloom object sizes, their geographical location and collocation
652 and timing. For the timing component the onset, duration, and demise of individual bloom objects
653 (events) could be considered. For the season all the identified space-time objects provided an estimate
654 of the onset, duration and end of the bloom season as a whole. The season was found to be of similar
655 length, but the onset was found to begin 26 days later in the AMM7v11 analyses than in the L4 product,
656 and the AMM7v11 analyses persist the season for almost a month beyond the diagnosed end identified
657 in the L4 product. Using traditional verification methods, data assimilation has been shown to

658 considerably reduce the delay in bloom onset in the model (~~Skákala et al., 2020~~)(Skákala et al., 2020).

659 Using feature-based verification methods, this study suggests that a substantial delay still remains.

660

661 There is a modest concentration bias in the AMM7v11 analyses compared to the L4 satellite ocean
662 colour product. In this study we chose not to mitigate against this bias as it was not considered to
663 impede the identification of bloom objects, which would prevent the ability of the methodology to
664 identify matches and create paired object statistics. Any concentration bias does affect the results and
665 this effect must be understood or at least kept in mind when interpreting results, in this case it will have
666 contributed to the result that the AMM7v11 bloom objects are generally larger. An alternative approach
667 would be to mitigate against the impact of the bias before using a threshold-based methodology such as
668 MODE or MTD. A quantile mapping approach is available within the MODE tool (not yet available in
669 MTD but should be available at some point) to remove the biases between two distributions as each
670 temporal data set is analysed. Using this method the one threshold is fixed and the other threshold varies
671 day-to-day (as shown in Figure 5). Another approach would be to analyse the bias for the whole season
672 (as shown in Figure 4) and deriving an equivalent threshold from this larger data set, thus applying a
673 fixed threshold to all the days in the season, though there would still be two different thresholds applied
674 to the two data sets.

675

676 MODE results suggest that the AMM7v11 bloom objects are larger than those in the L4 product.
677 AMM7v11 produces more objects (in number) than seen in the L4 ocean colour product, yet many of
678 the coastal objects seen in the L4 product are not as well resolved in AMM7v11 due to the coarseness of
679 the coastline in the 7 km model. The additional AMM7v11 objects are mainly found in deeper Atlantic
680 waters. The diagnosis of coastal blooms should improve if the model resolution were increased from
681 7 km to 1.5 km.

682

683 Using MODE and MTD clearly gives extra information not obtained from traditional verification
684 metrics that are more routinely used (McEwan et al., 2021). An alternative approach to assessing the
685 representation of phytoplankton blooms might be to use phenological indices (Siegel et al., 2002;

686 Soppa, et al., 2016), which measure the day of the year on which Chl-*a* concentration first crosses a
687 threshold based on the median concentration. Phenological indices have been used in observation
688 process studies (Racault et al., 2012), but very rarely for model verification, and then only in 1D
689 (Anugerahanti et al., 2018). One reason for this is that daily model Chl-*a* will frequently cross such a
690 threshold throughout the bloom season, meaning temporal smoothing and other processing (Cole et al.,
691 2012) would be required, which is not straightforward to apply consistently. Objective methods such as
692 MODE and MTD, which consider individual bloom objects throughout the season, rather than assuming
693 a single spring bloom will occur at each location, bypass these difficulties.

694

695 Other work that formed part of this study, but is not reported on here, showed that constraining the Chl-
696 *a* using assimilation of the satellite observations appears to benefit the model in terms of fewer
697 unmatched bloom regions. This should translate to an improvement in the forecasts generated from this
698 analysis compared with previous versions of the operational system and will be the subject of future
699 work.

700 **6. Code availability**

701 Model Evaluation Tools (MET) was initially developed at the National Center for Atmospheric
702 Research (NCAR) through grants from the National Science Foundation (NSF), the National Oceanic
703 and Atmospheric Administration (NOAA), the United States Air Force (USAF) and the United States
704 Department of Energy (DOE). The tool is now open source and available for download on github:
705 <https://github.com/dtcenter/MET>. For this study MET version 8.1 of the software was used. MET
706 allows for a variety of input file formats but some pre-processing of the CMEMS NetCDF files was
707 necessary before the MODE package could be applied. This includes regridding of the observations
708 onto the model grid, and addition of the forecast reference time variables to the NetCDF attributes. All
709 aspects on the use of MET are provided in in the MET software documentation available online at
710 <https://dtcenter.github.io/MET>.

711 **7. Data availability**

712 Data used in this paper was downloaded from the Copernicus Marine and Environment Monitoring
713 Service (CMEMS). The datasets used were:

- 714 • [https://resources.marine.copernicus.eu/?option=com_csw&task=results?option=com_csw&view=de](https://resources.marine.copernicus.eu/?option=com_csw&task=results?option=com_csw&view=details&product_id=OCEANCOLOUR_ATL_CHL_L4_NRT_OBSERVATIONS_009_037)
715 [tails&product_id=OCEANCOLOUR_ATL_CHL_L4_NRT_OBSERVATIONS_009_037](https://resources.marine.copernicus.eu/?option=com_csw&task=results?option=com_csw&view=details&product_id=OCEANCOLOUR_ATL_CHL_L4_NRT_OBSERVATIONS_009_037) (last
716 access: August 2019),
- 717 • [https://resources.marine.copernicus.eu/?option=com_csw&view=details&product_id=NORTHWES](https://resources.marine.copernicus.eu/?option=com_csw&view=details&product_id=NORTHWESTSHELF_ANALYSIS_FORECAST_BIO_004_002_b)
718 [TSHELF_ANALYSIS_FORECAST_BIO_004_002_b](https://resources.marine.copernicus.eu/?option=com_csw&view=details&product_id=NORTHWESTSHELF_ANALYSIS_FORECAST_BIO_004_002_b) (last access: August 2019)

719

720 The AMM7v11 analyses were not operational at the time of this study and not yet available from the
721 CMEMS server.

722 **8. Author contribution**

723 All authors contributed to the introduction, data and methods, and conclusions. MM, RN, JM and CP
724 contributed to the scientific evaluation and analysis of the results. MM and RN designed and ran the
725 model assessments. CP supported the assessments through the provision and reformatting of the data
726 used. DF provided detail on the model configurations used.

727 **9. Competing interests**

728 The authors declare that they have no conflict of interest.
729

730 **10. Acknowledgements**

731 This study has been conducted using E.U. Copernicus Marine Service Information.

732

733 This work has been carried out as part of the Copernicus Marine Environment Monitoring Service
734 (CMEMS) HiVE project. CMEMS is implemented by Mercator Ocean International in the framework
735 of a delegation agreement with the European Union.

736

737 We would like to thank the National Center for Atmospheric Research (NCAR) Developmental Testbed
738 Center (DTC) for the help received via their met_help facility in getting MET to work with ocean data,
739 and Robert McEwan (Met Office) for his assistance with the production of the traditional metrics.

740 **11. References**

741 Allen, J. I. and Somerfield, P. J.: A multivariate approach to model skill assessment, *J. Mar. Syst.*,
742 76(1–2), doi:10.1016/j.jmarsys.2008.05.009, 2009.

743 Allen, J. I., Holt, J. T., Blackford, J. and Proctor, R.: Error quantification of a high-resolution coupled
744 hydrodynamic-ecosystem coastal-ocean model: Part 2. Chlorophyll-a, nutrients and SPM, *J. Mar. Syst.*,
745 68(3–4), doi:10.1016/j.jmarsys.2007.01.005, 2007a.

746 Allen, J. I., Somerfield, P. J. and Gilbert, F. J.: Quantifying uncertainty in high-resolution coupled
747 hydrodynamic-ecosystem models, *J. Mar. Syst.*, 64(1–4), doi:10.1016/j.jmarsys.2006.02.010, 2007b.

748 Antoine, D., Andrt, J. M. and Morel, A.: Oceanic primary production: 2. Estimation at global scale from
749 satellite (Coastal Zone Color Scanner) chlorophyll, *Global Biogeochem. Cycles*, 10(1),
750 doi:10.1029/95GB02832, 1996.

751 Anugerahanti, P., Roy, S. and Haines, K.: A perturbed biogeochemistry model ensemble evaluated
752 against in situ and satellite observations, *Biogeosciences Discuss.*, doi:10.5194/bg-2018-136, 2018.

753 Behrenfeld, M. J., Boss, E., Siegel, D. A. and Shea, D. M.: Carbon-based ocean productivity and
754 phytoplankton physiology from space, *Global Biogeochem. Cycles*, 19(1), doi:10.1029/2004GB002299,
755 2005.

756 Bruggeman, J. and Bolding, K.: A general framework for aquatic biogeochemical models, *Environ.*
757 *Model. Softw.*, 61, doi:10.1016/j.envsoft.2014.04.002, 2014.

758 Butenschön, M., Clark, J., Aldridge, J. N., Icarus Allen, J., Artioli, Y., Blackford, J., Bruggeman, J.,
759 Cazenave, P., Ciavatta, S., Kay, S., Lessin, G., Van Leeuwen, S., Van Der Molen, J., De Mora, L.,

760 Polimene, L., Sailley, S., Stephens, N. and Torres, R.: ERSEM 15.06: A generic model for marine
761 biogeochemistry and the ecosystem dynamics of the lower trophic levels, *Geosci. Model Dev.*, 9(4),
762 doi:10.5194/gmd-9-1293-2016, 2016.

763 Chelton, D. B., Schlax, M. G. and Samelson, R. M.: Global observations of nonlinear mesoscale eddies,
764 *Prog. Oceanogr.*, 91(2), doi:10.1016/j.pocean.2011.01.002, 2011.

765 Chiswell, S. M.: Annual cycles and spring blooms in phytoplankton: Don't abandon Sverdrup
766 completely, *Mar. Ecol. Prog. Ser.*, 443, doi:10.3354/meps09453, 2011.

767 Clark, A. J., Bullock, R. G., Jensen, T. L., Xue, M. and Kong, F.: Application of object-based time-
768 domain diagnostics for tracking precipitation systems in convection-allowing models, *Weather*
769 *Forecast.*, 29(3), doi:10.1175/WAF-D-13-00098.1, 2014.

770 [Cole, H., Henson, S., Martin, A., and Yool, A.: Mind the gap: The impact of missing data on the](#)
771 [calculation of phytoplankton phenology metrics, *J. Geophys. Res.*, 117\(C08030\),](#)
772 [doi:doi:10.1029/2012JC008249, 2012.](#)

773 Crocker, R., Maksymczuk, J., Mittermaier, M., Tonani, M. and Pequignet, C.: An approach to the
774 verification of high-resolution ocean models using spatial methods, *Ocean Sci.*, 16(4), doi:10.5194/os-
775 16-831-2020, 2020.

776 Crocker, R. L. and Mittermaier, M. P.: Exploratory use of a satellite cloud mask to verify {NWP}
777 models, *Meteorol. Appl.*, 20, 197–205, 2013.

778 Davis, C., Brown, B. and Bullock, R.: Object-based verification of precipitation forecasts, Part {I}:
779 Methods and application to mesoscale rain areas, *Mon. Wea. Rev.*, 134, 1772–1784, 2006.

780 Dorninger, M., Gilleland, E., Casati, B., Mittermaier, M., Ebert, E., Brown, B. and Wilson, L.: The set-
781 up of the {M}esoscale {V}erification{I}nter-Comparison over {C}omplex {T}errain ({M}eso{VICT})
782 project, *Bull. Amer. Meteorol. Soc.*, 2018.

783 Dutkiewicz, S., Hickman, A. E. and Jahn, O.: Modelling ocean-colour-derived chlorophyll A,
784 *Biogeosciences*, 15(2), doi:10.5194/bg-15-613-2018, 2018.

785 Edwards, K. P., Barciela, R. and Butenschön, M.: Validation of the NEMO-ERSEM operational
786 ecosystem model for the North West European continental shelf, *Ocean Sci.*, 8(6), doi:10.5194/os-8-
787 983-2012, 2012.

788 Falkowski, P. G., Barber, R. T. and Smetacek, V.: Biogeochemical controls and feedbacks on ocean
789 primary production, *Science* ~~(80-.)~~_{..2}, 281(5374), doi:10.1126/science.281.5374.200, 1998.

790 Ford, D. A., Van Der Molen, J., Hyder, K., Bacon, J., Barciela, R., Creach, V., McEwan, R., Ruardij, P.
791 and Forster, R.: Observing and modelling phytoplankton community structure in the North Sea,
792 *Biogeosciences*, 14(6), doi:10.5194/bg-14-1419-2017, 2017.

793 Gilleland, E., Ahijevych, D., Brown, B. and Ebert, E.: Intercomparison of Spatial Forecast Verification
794 Methods, *Wea. Forecast.*, 24, 2009.

795 Gilleland, E., Lindström, J. and Lindgren, F.: Analyzing the image warp forecast verification method on
796 precipitation fields from the {ICP}, *Weather Forecast.*, 25(4), 1249–1262, 2010.

797 Gordon, H. R., Clark, D. K., Brown, J. W., Brown, O. B., Evans, R. H. and Broenkow, W. W.:
798 Phytoplankton pigment concentrations in the Middle Atlantic Bight: comparison of ship determinations
799 and CZCS estimates, *Appl. Opt.*, 22(1), doi:10.1364/ao.22.000020, 1983.

800 Hausmann, U. and Czaja, A.: The observed signature of mesoscale eddies in sea surface temperature
801 and the associated heat transport, *Deep. Res. Part I Oceanogr. Res. Pap.*, 70,
802 doi:10.1016/j.dsr.2012.08.005, 2012.

803 Hipsey, M. R., Gal, G., Arhonditsis, G. B., Carey, C. C., Elliott, J. A., Frassl, M. A., Janse, J. H., de
804 Mora, L. and Robson, B. J.: A system of metrics for the assessment and improvement of aquatic
805 ecosystem models, *Environ. Model. Softw.*, 128, doi:10.1016/j.envsoft.2020.104697, 2020.

806 [ICES: Dataset on Ocean Hydrography, \[online\] Available from: http://ocean.ices.dk/HydChem/, 2014.](http://ocean.ices.dk/HydChem/)

807 Jolliff, J. K., Kindle, J. C., Shulman, I., Penta, B., Friedrichs, M. A. M., Helber, R. and Arnone, R. A.:
808 Summary diagrams for coupled hydrodynamic-ecosystem model skill assessment, *J. Mar. Sys.*, 76, 64–
809 82, 2009.

810 King, R. R., While, J., Martin, M. J., Lea, D. J., Lemieux-Dudon, B., Waters, J. and O’Dea, E.:
811 Improving the initialisation of the Met Office operational shelf-seas model, *Ocean Model.*, 130,
812 doi:10.1016/j.ocemod.2018.07.004, 2018.

813 LORENZEN, C. J.: SURFACE CHLOROPHYLL AS AN INDEX OF THE DEPTH, CHLOROPHYLL
814 CONTENT, AND PRIMARY PRODUCTIVITY OF THE EUPHOTIC LAYER, *Limnol. Oceanogr.*,
815 15(3), doi:10.4319/lo.1970.15.3.0479, 1970.

816 Madec, G. and the N. team: Nemo Engine., 2016.

817 Mass, C. F., Ovens, D., Westrick, K. and Colle, B. A.: Does increasing horizontal resolution produce
818 more skillful forecasts? The results of two years of real-time numerical weather prediction over the
819 Pacific northwest, *Bull. Amer. Meteorol. Soc.*, 83(3), 407–430, 2002.

820 [Mattern, J.P.; Fennel, K.; Dowd, M.: Introduction and Assessment of Measures for Quantitative Model-](#)
821 [Data Comparison Using Satellite Images.No Title, *Remote Sens.*, 2, 794–818 \[online\] Available from:](#)
822 <https://doi.org/10.3390/rs2030794>., 2010.

823 [McEwan, Robert, Kay, Susan, & Ford, D.: CMEMS-NWS-QUID-004-002 \(Version 4.2\). \[online\]](#)
824 [Available from: http://doi.org/10.5281/zenodo.4746438](http://doi.org/10.5281/zenodo.4746438)., 2021.

825 Mittermaier, M. and Bullock, R.: Using {MODE} to explore the spatial and temporal characteristics of
826 cloud cover forecasts from high-resolution {NWP} models, *Meteorol. Appl.*, 20, 187–196, 2013.

827 Mittermaier, M., North, R., Semple, A. and Bullock, R.: Feature-based diagnostic evaluation of global
828 NWP forecasts, *Mon. Wea. Rev.*, 144(10), Submitted, 2016.

829 Moore, T. S., Campbell, J. W. and Dowell, M. D.: A class-based approach to characterizing and
830 mapping the uncertainty of the MODIS ocean chlorophyll product, *Remote Sens. Environ.*, 113(11),
831 2424–2430, doi:<https://doi.org/10.1016/j.rse.2009.07.016>, 2009.

832 De Mora, L., Butenschön, M. and Allen, J. I.: The assessment of a global marine ecosystem model on
833 the basis of emergent properties and ecosystem function: A case study with ERSEM, *Geosci. Model*
834 *Dev.*, 9(1), doi:10.5194/gmd-9-59-2016, 2016.

835 Morrow, R. and Le Traon, P. Y.: Recent advances in observing mesoscale ocean dynamics with satellite
836 altimetry, *Adv. Sp. Res.*, 50(8), doi:10.1016/j.asr.2011.09.033, 2012.

837 O’Dea, E. J., Arnold, A. K., Edwards, K. P., Furner, R., Hyder, P., Martin, M. J., Siddorn, J. R.,
838 Storkey, D., While, J., Holt, J. T. and Liu, H.: An operational ocean forecast system incorporating
839 NEMO and SST data assimilation for the tidally driven European North-West shelf, *J. Oper. Oceanogr.*,
840 5(1), doi:10.1080/1755876X.2012.11020128, 2012.

841 ~~O’Dea~~O’Dea, E., Furner, R., Wakelin, S., Siddorn, J., While, J., Sykes, P., King, R., Holt, J.
842 and Hewitt, H.: The CO5 configuration of the 7 km Atlantic Margin Model: Large scale
843 biases and sensitivity to forcing, physics options and vertical resolution, *Geosci. Model Dev. Discuss.*,

844 doi:10.5194/gmd-2017-15, 2017.

845 [Racault, M. F., Le Quéré, C., Buitenhuis, E., Sathyendranath, S., & Platt, T.: Phytoplankton phenology](#)
846 [in the global ocean, *Ecol. Indic.*, 14\(1\), 152–163, 2012.](#)

847 Rossa, A. M., Nurmi, P. and Ebert, E. E.: Precipitation: Advances in Measurement, Estimation and
848 Prediction, pp. 418–450, Springer., 2008.

849 Saux Picart, S., Butenschén, M. and Shutler, J. D.: Wavelet-based spatial comparison technique for
850 analysing and evaluating two-dimensional geophysical model fields, *Geosci. Model Dev.*, 5(1),
851 doi:10.5194/gmd-5-223-2012, 2012.

852 Schalles, J. F.: Optical remote sensing techniques to estimate phytoplankton chlorophyll a
853 concentrations in coastal waters with varying suspended matter and cdom concentrations, in *Remote*
854 *Sensing and Digital Image Processing*, vol. 9., 2006.

855 Shutler, J. D., Smyth, T. J., Saux-Picart, S., Wakelin, S. L., Hyder, P., Orekhov, P., Grant, M. G.,
856 Tilstone, G. H. and Allen, J. I.: Evaluating the ability of a hydrodynamic ecosystem model to capture
857 inter- and intra-annual spatial characteristics of chlorophyll-a in the north east Atlantic, *J. Mar. Syst.*,
858 88(2), doi:10.1016/j.jmarsys.2011.03.013, 2011.

859 Siegel, D. A., Doney, S. C. and Yoder, J. A.: The North Atlantic Spring Phytoplankton Bloom and
860 [Sverdrup's Critical Depth Hypothesis](#), *Science* (80-.), 296(5568), 730–733,
861 doi:10.1126/science.1069174, 2002.

862 Skákala, J., Ford, D., Brewin, R. J. W., McEwan, R., Kay, S., Taylor, B., de Mora, L. and Ciavatta, S.:
863 The Assimilation of Phytoplankton Functional Types for Operational Forecasting in the Northwest
864 European Shelf, *J. Geophys. Res. Ocean.*, 123(8), 5230–5247, doi:10.1029/2018JC014153, 2018.

865 Skákala, J., Bruggeman, J., Brewin, R. J. W., Ford, D. A. and Ciavatta, S.: Improved Representation of
866 Underwater Light Field and Its Impact on Ecosystem Dynamics: A Study in the North Sea, *J. Geophys.*
867 *Res. Ocean.*, 125(7), e2020JC016122, doi:10.1029/2020JC016122, 2020.

868 Smyth, T. J., Allen, I., Atkinson, A., Bruun, J. T., Harmer, R. A., Pingree, R. D., Widdicombe, C. E.
869 and Somerfield, P. J.: Ocean net heat flux influences seasonal to interannual patterns of plankton
870 abundance, *PLoS One*, 9(6), e98709, doi:10.1371/journal.pone.0098709, 2014.

871 [Soppa, M.A.; Völker, C.; Bracher, A.: Diatom Phenology in the Southern Ocean: Mean Patterns, Trends](#)

872 [and the Role of Climate Oscillations, Remote Sens., 8\(420\), doi:https://doi.org/10.3390/rs8050420,](https://doi.org/10.3390/rs8050420)
873 [2016.](https://doi.org/10.3390/rs8050420)

874 Stow, C. A., Jolliff, J., McGillicuddy, D. J., Doney, S. C., Allen, J. I., Friedrichs, M. A. M., Rose, K. A.
875 and Wallhead, P.: Skill assessment for coupled biological/physical models of marine systems, *J. Mar.*
876 *Syst.*, 76(1–2), doi:10.1016/j.jmarsys.2008.03.011, 2009.

877 Sverdrup, H. U.: On conditions for the vernal blooming of phytoplankton, *ICES J. Mar. Sci.*, 18(3),
878 doi:10.1093/icesjms/18.3.287, 1953.

879 Taylor, K. E.: Summarizing multiple aspects of model performance in a single diagram, *J. Geophys.*
880 *Res. Atmos.*, 106(D7), doi:10.1029/2000JD900719, 2001.

881 Le Traon, P. Y., Reppucci, A., Fanjul, E. A., Aouf, L., Behrens, A., Belmonte, M., Bentamy, A.,
882 Bertino, L., Brando, V. E., Kreiner, M. B., Benkiran, M., Carval, T., Ciliberti, S. A., Claustre, H.,
883 Clementi, E., Coppini, G., Cossarini, G., De Alfonso Alonso-Muñoyerro, M., Delamarche, A.,
884 Dibarboure, G., Dinessen, F., Drevillon, M., Drillet, Y., Faugere, Y., Fernández, V., Fleming, A.,
885 Garcia-Hermosa, M. I., Sotillo, M. G., Garric, G., Gasparin, F., Giordan, C., Gehlen, M., Gregoire, M.
886 L., Guinehut, S., Hamon, M., Harris, C., Hernandez, F., Hinkler, J. B., Hoyer, J., Karvonen, J., Kay, S.,
887 King, R., Lavergne, T., Lemieux-Dudon, B., Lima, L., Mao, C., Martin, M. J., Masina, S., Melet, A.,
888 Nardelli, B. B., Nolan, G., Pascual, A., Pistoia, J., Palazov, A., Piolle, J. F., Pujol, M. I., Pequignet, A.
889 C., Peneva, E., Gómez, B. P., de la Villeon, L. P., Pinardi, N., Pisano, A., Pouliquen, S., Reid, R.,
890 Remy, E., Santoleri, R., Siddorn, J., She, J., Staneva, J., Stoffelen, A., Tonani, M., Vandenbulcke, L.,
891 von Schuckmann, K., Volpe, G., Wettre, C. and Zacharioudaki, A.: From observation to information
892 and users: The Copernicus Marine Service Perspective, *Front. Mar. Sci.*, 6(May),
893 doi:10.3389/fmars.2019.234, 2019.

894 Vichi, M., Allen, J. I., Masina, S. and Hardman-Mountford, N. J.: The emergence of ocean
895 biogeochemical provinces: A quantitative assessment and a diagnostic for model evaluation, *Global*
896 *Biogeochem. Cycles*, 25(2), doi:10.1029/2010GB003867, 2011.

897 Waters, J., Lea, D. J., Martin, M. J., Mirouze, I., Weaver, A. and While, J.: Implementing a variational
898 data assimilation system in an operational 1/4 degree global ocean model, *Q. J. R. Meteorol. Soc.*,
899 141(687), 333–349, doi:10.1002/qj.2388, 2015.

900 Winder, M. and Cloern, J. E.: The annual cycles of phytoplankton biomass, *Philos. Trans. R. Soc. B*
901 *Biol. Sci.*, 365(1555), doi:10.1098/rstb.2010.0125, 2010.

902

903